Remote Sensing of Environment 297 (2023) 113790

Contents lists available at ScienceDirect

Remote Sensing of Environment

journal homepage: www.elsevier.com/locate/rse

Monitoring spring leaf phenology of individual trees in a temperate forest fragment with multi-scale satellite time series

Yilun Zhao [a], Chunyuan Diao [a,*], Carol K. Augspurger [b], Zijun Yang [a]

[a] Department of Geography & Geographic Information Science, University of Illinois at Urbana-Champaign, Urbana, IL 61801, USA
[b] Department of Plant Biology, University of Illinois at Urbana-Champaign, Urbana, IL 61801, USA

ARTICLE INFO

Edited by Marie Weiss

Keywords:
Forest fragment
PlanetScope
Multi-scale satellite time series
Spring leaf phenology
Field observations

ABSTRACT

Forest fragmentation has been increasingly exacerbated by deforestation, urbanization, and agricultural expansion. Monitoring the forest fragments via the lens of tree-crown scale leaf phenology is critical to understand tree species phenological responses to climate change and identify the fragment species vulnerable to environmental disturbance. Despite advances in remote sensing for phenology monitoring, detecting tree-crown scale leaf phenology in fragmented forests remains challenging. Simultaneous tracking of key spring phenological events that are crucial to ecosystem functions and climate change responses is also neglected. To address these challenges, we develop a novel tree-crown scale remote sensing phenological monitoring framework to characterize all the critical spring phenological events of individual trees of deciduous forest fragments, with Trelease Woods in Champaign, Illinois as a case study. The novel framework comprises four components: 1) generate high spatiotemporal resolution fusion imagery from multi-scale satellite time series with a hybrid deep learning fusion model; 2) calibrate PlanetScope imagery time series with fusion data using histogram matching; 3) model tree-crown scale phenology trajectory with a Beck logistic-based method; 4) detect a diversity of tree-crown scale phenological events using several phenological metric extraction methods (i.e., threshold- and curve feature-based methods). Combined with weekly in-situ phenological observations of 123 individual trees across 12 broadleaf species from 2017 to 2020, the framework effectively bridges the satellite- and field-based phenological measures for the key spring phenological events (i.e., budswell, budburst, leaf expansion, and leaf maturity events) at the tree-crown scale, particularly for large individuals (RMSE <1 week for most events). Calibration of PlanetScope imagery using multi-scale satellite fusion data in consideration of landscape fragmentation is critical for monitoring tree phenology of forest fragments. Compared to curve feature-based methods, threshold-based phenometric extraction methods demonstrate enhanced capability in detecting spring leaf phenological dynamics of individual trees. Among the phenological events, full leaf out and early leaf expansion events are retrieved with high accuracy using calibrated PlanetScope time series (RMSE from 3 to 5 days and R-squared higher than 0.8). With both intensive satellite and field phenological efforts, this novel framework is at the forefront of interpreting tree-crown scale remotely sensed phenological metrics in the context of biologically meaningful field phenological events in fragmented forest setting.

1. Introduction

In recent decades, forest loss has increased substantially with the continuing urban growth, cropland expansion, community-driven deforestation, and more frequent wildfire (Curtis et al., 2018; van Vliet, 2019; van Wees et al., 2021). Forest loss is usually concomitant with fragmentation, in which a large patch of forest is separated into many small fragments by farmlands or settlements. A forest fragment, also known as a forest remnant or patch, is generally defined as a relatively small, isolated area of forest that is surrounded by a matrix of other land uses (e.g., agricultural fields and pastures) (Bryan-Brown et al., 2020; Gibson et al., 2013; Taubert et al., 2018). Forest fragments, despite their sizes being much smaller than those of large forests, play an important role as the shelter for wildlife, the travelling corridor of migrant animals, and the recreational areas for human beings (Aguilar-Melo et al., 2013; Amaya-Espinel and Hostetler, 2019; dos Santos et al., 2020). Given the increasing difficulty of maintaining large, contiguous forests, it becomes more critical to protect and closely monitor the

* Corresponding author.
E-mail address: chunyuan@illinois.edu (C. Diao).

https://doi.org/10.1016/j.rse.2023.113790
Received 21 February 2023; Received in revised form 20 August 2023; Accepted 25 August 2023
Available online 1 September 2023

remaining forest fragments, particularly their responses to environmental disturbances. Such responses of forest fragments can be monitored via multiple metrics, including plant richness, forest biomass, and tree leaf phenology. Among those metrics, leaf phenology is the study of periodic life phases (e.g., budswell, budburst, and leaf expansion) of plant leaves. The timing of these events is affected by a combination of environmental factors (e.g., temperature, precipitation, and photoperiod) (Dai et al., 2014; Morin et al., 2010; Xie et al., 2018; Zhang et al., 2003). Compared to contiguous forests, forest fragments often exhibit altered leaf phenology, largely due to differences in microclimate, edge effects, and species composition (Fernando et al., 2015; Hofmeister et al., 2019; Meier and Leuschner, 2008). Monitoring the leaf phenology of forest fragments also facilitates the quantification of the magnitude, timing, and phase of net ecosystem exchange of CO_2 between plants and the atmosphere, thus enhancing our understanding of how climate change influences ecosystem functions of fragmented forests through affecting carbon, nutrient, and water cycles (Ahrends et al., 2009).

Leaf phenology among individual trees within a forest fragment (or community) is usually not synchronous and shows high interspecific and intraspecific variation (Donnelly et al., 2017; Liu et al., 2011; Sun et al., 2006). The tree phenology variation in spring, caused by a combination of environmental factors (e.g., winter chill, spring temperature, and photoperiod), results in staggering and asynchronous phenological development among individual trees within a forest fragment. Given the different phenological responses of tree species to climate change, a forest fragment may be subject to species invasion if the tree phenology of species and individuals in the fragment is shifted to similar timing under future climate (Willis et al., 2010; Wolkovich et al., 2013). Increased phenological synchronization may offer periods of resource surplus, which invasive species with flexible growth strategies may exploit to gain a foothold. Monitoring the tree-crown scale leaf phenology of a fragmented forest facilitates the understanding of species phenological responses to environmental and climate change, aiding in forest and invasive species management under such change. It can also help identify the tree species that are vulnerable to environmental disturbances (e.g., disease, pest infestation, and drought). The changes in leaf phenology patterns (e.g., delayed leafing or reduced phenological development rate) may provide early warning signs of stress in individual trees caused by the disturbances (Chen et al., 2017; Evans et al., 2012). Monitoring the tree-crown scale leaf phenology can further help infer the potential shifts in species distributions under climate change, as altered leaf phenology (e.g., earlier leaf emergence) caused by the change of climate conditions (e.g., temperature) may enable species to expand their distribution into areas where climate becomes favorable, or species may face challenges if the phenological changes (e.g., relatively delayed leaf development) are disadvantageous (Donnelly et al., 2017; Öztürk et al., 2015; Willis et al., 2010; Wolkovich et al., 2013).

Tree leaf phenology can be monitored via both intensive in situ phenological observations and the collection of time series of remote sensing imagery. In situ observations provide accurate timing of tree phenological events, but they are time- and resource-consuming and usually require much field experience. In recent years, remote sensing has been utilized increasingly to monitor leaf phenology from local to global scales (Bolton et al., 2020; Diao, 2019; Dronova and Taddeo, 2022; Fawcett et al., 2021; Matongera et al., 2021). Remote monitoring of leaf phenology typically involves three main steps (Berra and Gaulton, 2021; Diao, 2020; Zeng et al., 2020). The first step is to mitigate the negative effects of sensing noises and outliers (e.g., abnormal values caused by cloud, snow, and/or soil background) through pre-processing of the remote sensing time series, which includes the use of maximum value composite (MVC) method and filtering methods (e.g., night filter and spline filter) (Berra and Gaulton, 2021; Filippa et al., 2016). The second step is to model the leaf phenological development trajectory via phenological curve fitting to the pre-processed remote sensing time series. The phenological curve fitting functions include double logistic function (Beck et al., 2006; Cao et al., 2015; Elmore et al., 2012), quadratic function (de Beurs and Henebry, 2004), asymmetric Gaussian function (Jönsson and Eklundh, 2004), and Savitzky-Golay function (Chen et al., 2004). The third step is to characterize the leaf phenological events via the retrieval of phenological metrics from the fitted time series. The phenological metric extraction methods can generally be grouped into two categories, namely threshold-based methods (e.g., absolute and relative thresholds) and curve feature-based methods (e.g., derivative and curvature change rate methods) (Berra and Gaulton, 2021; Zeng et al., 2020). Tree-crown scale leaf phenology, with its fine spatial resolution requirements, may be monitored using drone, phenocam, or high-resolution satellite time series. However, the labor-intensive nature of drone imagery collection and the limited number of individual trees included in the view of phenocams make the use of these two sources in tree phenology monitoring difficult at large scales. The newly launched PlanetScope satellites, with their global coverage data of an approximate 3-m spatial resolution and near daily temporal resolution, open up unique opportunities to capture diverse plant phenological development trajectories at the tree-crown scale. Such potential is still underexplored, given the challenges of simultaneously acquiring systematic high-quality satellite and field phenological measures of individual trees, in combination with the radiometric inconsistency among the PlanetScope sensors.

Apart from the difficulty in monitoring tree-crown scale leaf phenology using remote sensing, the leaf phenological events characterized by remotely sensed phenological metrics are also quite limited. During the spring season, the remotely sensed phenological metrics are typically utilized to approximate the timing of budburst (leaf out), a phenological event indicative of the start of the growing season (Berra and Gaulton, 2021; Bórnez et al., 2020; Zhang et al., 2020). However, each component of spring tree phenology events (e.g., onset and completion of budswell, budburst, leaf expansion, and leaf maturity phases) should be closely monitored as each has important ecosystem functions and responds differently to climate change. For example, the timing of tree budburst (leaf out) is closely related to the onset of carbon sequestration, biomass accumulation and timber production, and is usually advanced by warm spring and delayed by warm winter (Donnelly et al., 2017; Fridley, 2012; Keenan et al., 2014a, 2014b; Panchen et al., 2014; Richardson et al., 2018a, 2018b; Song et al., 2020). The timing of leaf expansion, which is sensitive to air and soil temperature, affects the maximum leaf area a tree crown can reach in spring, thus influencing forest canopy light interception, evapotranspiration, and summer canopy shade sizes (Chang, 2006; Öztürk et al., 2015; Tyrväinen et al., 2005). The monitoring of all critical spring phenological events can also facilitate more comprehensive assessment of the influence of environmental disturbances on a forest fragment. The altered spring phenological patterns caused by environmental disturbances may provide critical signs of species stress as well as changes in species interactions (e.g., species competition for resources), further affecting forest species composition and functions (e.g., carbon sequestration) (Flynn and Wolkovich, 2018; Smith, 2013; Willis et al., 2010; Wolkovich et al., 2013). During the spring season, the limited remotely sensed phenological characterization is mainly attributable to the challenge in bridging phenological metrics detected from satellite imagery with phenological events observed in situ. On the one hand, remotely sensed phenological metrics for characterizing the same field phenological event may vary with the use of different phenological metric extraction methods. For example, both threshold-based (e.g., 20–30% increase of vegetation index) and curve feature-based (e.g., local maximum in the curvature change rate) metric extraction methods have been employed for characterizing the leaf out event, with varying accuracies achieved (Gao et al., 2017; Jönsson and Eklundh, 2004; Kang et al., 2003; Klosterman et al., 2014; Tan et al., 2010; Vrieling et al., 2017, 2018). On the other hand, bridging of all critical leaf phenological events requires intensively systematic and consistent field phenological observations of a large number of trees throughout the entire spring season. Such intensive observations of all critical phenological events of

individual trees are not commonly made, but are crucial in connecting the satellite-based phenological metrics with the field-based ones for more comprehensive phenological characterization.

The goal of this study is to develop a tree-crown scale remote sensing phenological monitoring framework to characterize all the critical spring phenological events of individual trees in the fragmented forest setting. Using Trelease Woods in east-central Illinois, USA, (a temperate deciduous forest fragment located in heterogeneous landscapes) as a case study, the specific objectives are to: 1) calibrate the PlanetScope imagery time series with the fusion of multi-scale remote sensing data for extracting a wide range of phenological metrics at the tree-crown scale; 2) conduct intensive in-situ phenological observations that cover all the critical spring phenological events of a large number of individual trees of diverse species; 3) bridge the satellite- and field-based phenological measures of individual trees for characterizing remotely a diverse set of spring phenological events at the tree-crown scale.

2. Study site and data

2.1. Study site

This study is conducted in the north half of Trelease Woods (hereafter 'Trelease Woods') (Fig. 1). This 0.21 km^2 fragment of temperate deciduous forest is located in the northeast of Champaign County, Illinois, USA. Historically, Trelease Woods was part of the 'Big Grove', a large forest located to the northeast of Urbana prior to European settlement, and was occasionally disturbed by fires before the 1830s. In 1917, Trelease Woods was purchased by the University of Illinois and currently is one of only three remaining fragments of the Big Grove Forest. Historically, Trelease Woods was primarily a mature oak-hickory forest, but sugar maple (*Acer saccharum*) and elm (*Ulmus* spp.) species became the dominant tree species in the 20th century, presumably because of the decreasing fire frequency. Trelease Woods currently has moderately dense understory and a tall closed canopy with dead trees remaining standing. As a remnant of a large forest, now surrounded by urban settlements and agricultural fields, Trelease Woods is an excellent site for studying leaf phenology of individual trees in a fragmented forest setting. Tree phenology in both spring and autumn has been observed weekly by the same individual following the same monitoring protocol using binoculars in Trelease Woods from 1993 to 2022 (Augspurger and Zaya, 2022). These observations provide a wealth of ground-truth data for validating the phenological metrics detected using the corresponding remote sensing data, and ensure observation consistency for intra- and inter-specific phenological comparisons. In consideration of the PlanetScope data availability and drone imagery acquisition timing, we select the observations from 2017 to 2020 for all critical spring leaf phenological events of 12 deciduous tree species, with a total of 123 trees (Table 1).

Table 1
Summary of the study's tree species, number of individuals in each species, and number of large individuals (> 90 m^2) in each species.

Species	Number of Trees	Number of Large Trees
Ulmus americana (American Elm – AE)	2	0
Carya cordiformis (Bitternut Hickory – BH)	2	2
Quercus macrocarpa (Bur Oak – BO)	14	14
Celtis occidentalis (Common Hackberry – HB)	15	7
Gymnocladus dioicus (Kentucky Coffeetree - KCT)	8	0
Tilia americana (American Basswood – AB)	16	3
Aesculus glabra (Ohio Buckeye - OB)	12	0
Quercus rubra (Red Oak – RO)	11	11
Ulmus rubra (Slippery Elm – SE)	2	0
Carya laciniosa (Shellbark Hickory – SH)	12	7
Acer saccharum (Sugar Maple – SM)	11	5
Juglans nigra (Black Walnut - BW)	18	3

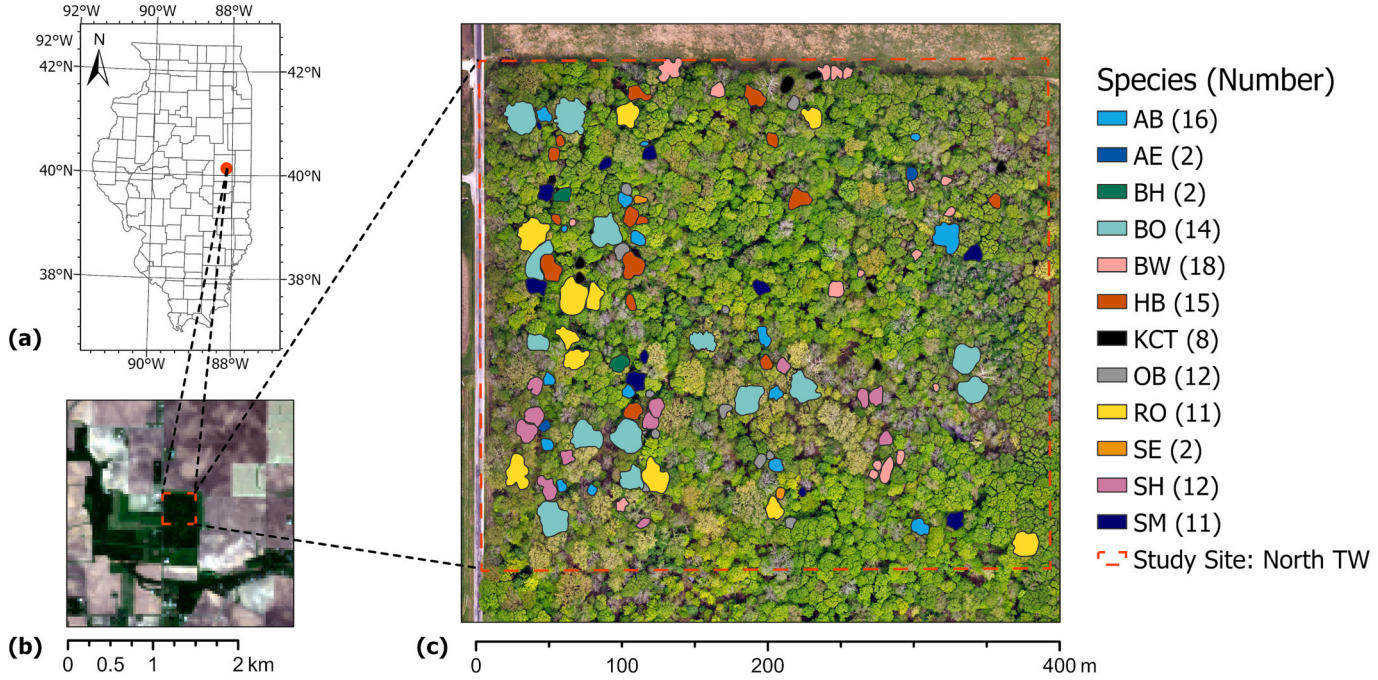

Fig. 1. (a) The location of the Trelease Woods study site. (b) The surrounding environment of Trelease Woods. (c) The tree crown boundaries of selected trees studied in Trelease Woods. The red dashed rectangle in (b) and (c) represents the study plot. Each polygon in (c) represents a tree crown with its boundary delineated using the drone imagery and visual interpretation. The scientific name of each species' abbreviation is in Table 1. In this study, we observe a total of 123 trees across 12 species: AB - *Tilia americana*, AE - *Ulmus americana*, BH - *Carya cordiformis*, BO - *Quercus macrocarpa*, BW - *Juglans nigra*, HB - *Celtis occidentalis*, KCT - *Gymnocladus dioicus*, OB - *Aesculus glabra*, RO - *Quercus rubra*, SE - *Ulmus rubra*, SH - *Carya laciniosa*, and SM - *Acer saccharum*. (For interpretation of the references to color in this figure legend, the reader is referred to the web version of this article.)

2.2. Data

In this study we acquire five types of data, including field phenological observation data, drone data, PlanetScope surface reflectance products, Harmonized Landsat Sentinel-2 (HLS) data, and Moderate Resolution Imaging Spectroradiometer (MODIS) surface reflectance products.

Our field data consist of day of year (DOY) of 10 field-collected spring phenological events (hereafter 'field events') of four phenological phases, namely budswell, budburst (or leaf out), leaf expansion, and mature phases. Budswell is the phase when the buds of a tree crown expand and reveal underlying parts of bud scales, typically changing to more distinct colors like green or reddish-brown. Though the tip of bud may show green, there is no shoot or leaf emergence at this phase. Budburst (or leaf out) corresponds to the phase when the buds of a tree crown open, and shoots or leaves start growth. Leaf expansion is the phase when the unfolded leaf blades of a crown expand until the full length. Leaf maturity corresponds to the date when leaves have 'hardened' and cease changing color, reaching their final green color. Except the mature phenological phase, each phase is characterized by three field events. Thus, the 10 field events collected include budswell 1, 2, and 3 (BS1, BS2, and BS3), budburst (or leaf out) 1, 2, and 3 (BB1, BB2, and BB3), leaf expansion 1, 2, and 3 (FE1, FE2, and FE3), and mature (MAT) events (Table 2). The 1, 2, and 3 events of a phase represent the completion of 1/3, 2/3, and all of the development phase, respectively. On a given census date, the phenological event documented represents the tree crown assessed as a whole (i.e., the dominant phenological state of all newly developing vegetative units across the entire crown). When a phenological event was not directly observed due to fluctuations in development speed, we estimated the date for each non-observed event using linear interpolation between dates with direct observations.

The 123 individuals observed in this study were randomly selected from the 12 most common and representative deciduous tree species in Trelease Woods (Fig. 1(c)). For example, bur oak (*Quercus macrocarpa*) and red oak (*Quercus rubra*) were observed as they have the largest and oldest trees of Trelease Woods, and sugar maple (*A. saccharum*) was observed because it is now the most dominant species. Selection of trees was designed for monitoring leaf phenology across the sizes of important species in Trelease Woods. In this study, tree crown sizes of 123 individuals range from 7.6 to 431.6 m^2. About 42% of individuals have relatively large tree crown sizes (i.e., $> 90\ m^2$); most large trees are from the dominant species (e.g., *Q. macrocarpa* and *Q. rubra*) (Table 1).

The drone images collected with DJI Matrice 100 in 2018 and 2019 are used as the reference for tree crown delineation. The drone images have three bands (i.e., Red, Green, and Blue bands) with a spatial resolution of 5 cm. The drone images were collected in 2018 on October 11, October 25, and November 2, and in 2019 on May 6, June 2, September 17, and November 4. All drone images first are aligned based on their GPS locations and orientations. The dense point cloud then is generated with the depth information from images collected by drone, and the digital elevation model (DEM) is built with the dense cloud points for generating orthomosaic images that are photogrammetrically orthorectified, color balanced, and seamless. The orthomosaic images on those observation dates are used as the reference for the further tree crown delineation process. All drone image processing steps, including drone image alignment, point cloud building, and orthomosaic image generation, are completed in Agisoft Metashape Professional.

The atmospherically corrected PlanetScope 4-band surface reflectance product with an approximate 3-m spatial resolution and a near-daily temporal resolution is used in this study. Its four bands are the Blue, Green, Red, and Near-infrared (NIR) bands. We acquire all available PlanetScope images with cloud covers lower than 40% before DOY 250 from 2017 to 2020. The DOY 250 is used as the cutoff date to cover the spring season (usually from DOY 85–160), as well as ensure the sufficient time span for tree crown-scale phenology modeling. To ensure the quality of PlanetScope data, the pixels contaminated by snow cover, cloud, cloud shadow, and haze are masked with the corresponding quality assurance layer (e.g., usable data mask [udm2]). In total, there are 18, 50, 55, and 70 cloud-free images of the study site from 2017 to 2020, respectively (Fig. 2). It is noted that the number of images available for target trees may be larger and varying after the masking. For example, the additional PlanetScope images of a multitude of days (e.g., DOY 13, 36, 48, 68, 105, and 116) are available for a range of target trees in 2017 besides the cloud-free images in Fig. 2. Since the PlanetScope constellation consists of >130 sensors, the PlanetScope images across sensors may suffer from radiometric inconsistency and are further calibrated in this study.

To decrease the radiometric inconsistency among the images collected by different PlanetScope sensors, the PlanetScope surface reflectance data are further calibrated using the MODIS and HLS fusion data. To generate the fusion data, we obtain all the HLS imagery of the study site (tile 16TCK) during the period of DOY 1–250 from 2017 to 2020. The HLS imagery is produced through the harmonization of Landsat 8, Sentinel-2A, and Sentinel-2B, which encompasses the atmospheric correction and cloud masking, spatial co-registration, Bidirectional Reflectance Distribution Function (BRDF) normalization, band pass adjustment, and temporal compositing (Claverie et al., 2018). The HLS imagery has a spatial resolution of 30-m and a temporal resolution of 2–3 days. To ensure the quality of the fusion data, the number of clear pixels within an HLS image is calculated with the quality assessment layer and only the images with the fraction of clear pixels >90% are selected for data fusion. In total, there are 7, 4, 5 and 7 HLS images selected from 2017 to 2020, respectively (Table 3).

We also collect all the MODIS Nadir BRDF-Adjusted Reflectance (NBAR) images (MCD43A4 h11v04 and h11v05, version 6) of the footprint of the HLS tile 16TCK for the same period (DOY 1–250) from 2017 to 2020 for generating the fusion data. The MODIS MCD43A4 imagery has a daily temporal resolution and 500-m spatial resolution. The reflectance at each date is generated by weighting all observations from Terra and Aqua sensors during the 16-day retrieval period in terms of image quality, observation coverage, and temporal distance to mitigate the influence of atmospheric interference and noise. With a kernel-driven semi-empirical BRDF model, the MCD43A4 accommodates the viewing angle effects to model the surface reflectance under a nadir view. This NBAR product can reduce the influence of BRDF on the leaf phenology monitoring (Wang et al., 2020). We further leverage the Terra Snow Cover Daily Global 500 m product (MOD10A1) to mask the corresponding snow pixels in MCD43A4. After masking the snow pixels, we re-sample the MODIS images to 30-m resolution of HLS using the bilinear interpolation and spatially align the re-sampled MODIS images

Table 2
Description of phenological events for each phenophase.

Code	Phase	Event	Description of Event (based on the status of the majority of buds or leaves of the tree crown)
BS	Budswell	1	Majority of buds are in 1/3 of their final sizes before bursting
		2	Majority of buds are in 2/3 of their final sizes before bursting
		3	Majority of buds are fully swollen (at final sizes)
BB	Budburst/ Leaf out	1	Budburst; for majority of buds, first leaf tips are visible beyond bud scales
		2	Majority of leaves/shoots emerge well beyond bud scales, but leaves are not yet unfolding and entire petioles are not visible
		3	Majority of individual leaf blades and petioles are visible; majority of leaves are unfolded but not expanded
FE	Leaf expansion	1	Majority of leaves are in 1/3 of their final sizes
		2	Majority of leaves are in 2/3 of their final sizes
		3	Majority of leaves are in their final sizes but not in final green color
MAT	Leaf maturity	1	Majority of leaves are in their final green color and appear thick and 'tough'

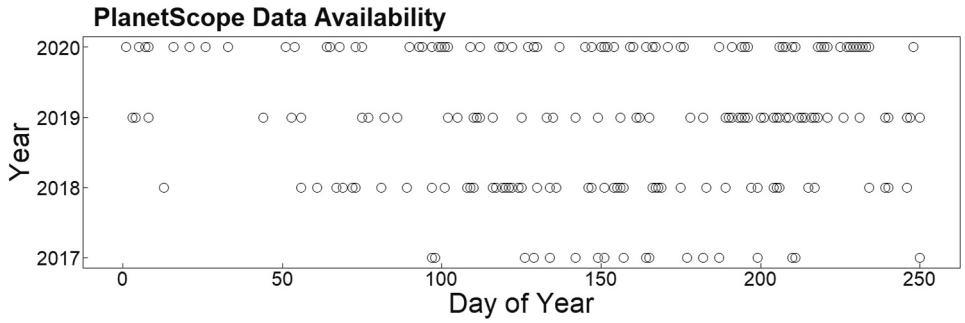

Fig. 2. The distribution of cloud-free PlanetScope data of DOY 1 to 250 from 2017 to 2020 in the study site.

Table 3
The day of year (source) of HLS images selected for generating the fusion data.

Year	Day of year (Source) of selected HLS images
2017	66(L30), 130(L30), 162(L30), 178(L30), 206(S30), 210(L30), 226(L30)
2018	101(L30), 117(L30), 206(S30), 213(L30)
2019	56(L30), 161(S30), 176(S30), 206(S30), 216(S30)
2020	1(S30), 123(L30), 166(S30), 187(L30), 211(S30), 219(L30), 231(S30)

with the HLS ones. Four bands (i.e., Blue, Green, Red, and NIR bands) of MODIS and HLS images are considered in the fusion process.

By fusing the HLS and corresponding MODIS data, we generate the MODIS-HLS fusion data with a spatial resolution of 30-m and daily temporal resolution. This fusion imagery of relatively high spatial and temporal resolutions is critical for calibrating the PlanetScope imagery of our study site, particularly in consideration of forest fragmentation, which otherwise cannot be achieved with the use of either MODIS or HLS data.

3. Methods

To monitor all the critical spring phenological events of individual trees in the fragmented forest setting, the framework proposed in this study includes four components: 1) generate high spatiotemporal resolution fusion imagery with multi-scale satellite time series, 2) calibrate PlanetScope imagery time series with the high spatiotemporal resolution fusion imagery, 3) model spring leaf phenology trajectory at the tree-crown scale using two-band Enhanced Vegetation Index (EVI2) time series of calibrated PlanetScope data, and 4) retrieve a multitude of tree-crown scale spring phenological events from modeled EVI2 time series (hereafter 'satellite events') and assess the retrieval accuracy with field events (Fig. 3).

3.1. Fusion of HLS and MODIS data with hybrid deep learning model

The hybrid deep learning model is employed to fuse MODIS and HLS images for generating the fusion image of 30-m spatial resolution and daily temporal resolution (Yang et al., 2021). For each prediction date, it generates the fusion image using the MODIS image on that date and two MODIS-HLS image pairs of surrounding dates. The image pair denotes the pair of MODIS and HLS images acquired on the same date. This hybrid deep learning model is selected for conducting the spatiotemporal image fusion owing to its robust performance in predicting varying levels of phenological changes among the imagery in heterogeneous landscapes. The fusion model hybridizes two types of deep learning modeling architectures, namely super-resolution convolutional neural network (SRCNN) and long short-term memory (LSTM). The SRCNN model extracts critical spatial features from the MODIS images and maps the extracted features to the HLS scale for reconstructing the corresponding super-resolution (SR) images. With the MODIS-HLS image pairs serving as the training dataset, the SRCNN model can register the reflectance of the MODIS and corresponding HLS images, as well as restore the degraded spatial details of the MODIS images in the derived SR images. The LSTM model learns the temporal reflectance changing patterns from the sequence of SR images derived from the SRCNN model. With the learned temporal patterns, it generates the final fusion image on the prediction date using the corresponding HLS images. The hybrid deep learning model is able to retrieve both the spatial relationship of the MODIS-HLS image pairs and the temporal changing patterns of the surface reflectance embedded in the time series images. Its ability to robustly model temporal changes among the imagery in heterogeneous landscapes makes this model especially suitable for generating the images for our fragmented forest site during the spring season when tree phenology undergoes rapid changes.

Specifically, the workflow of the hybrid deep learning model is shown in Fig. 4. Suppose that there are MODIS images M_{t-1}, M_t, and M_{t+1} collected on dates t-1, t, and $t+1$, respectively, and HLS images H_{t-1} and H_{t+1} collected on dates t-1 and $t+1$, respectively. With all these images, the hybrid model will estimate the fusion image on date t using the integration of SRCNN and LSTM. In the training process, the SRCNN model first takes the image pairs $M_{t-1} \sim H_{t-1}$ and $M_{t+1} \sim H_{t+1}$ for learning the spatial relationship between MODIS and HLS images, aiming to reconstruct HLS-wise SR images from the MODIS images. With the trained SRCNN model, the SR images on dates t-1, t and $t+1$ (i.e., SR_{t-1}, SR_t, and SR_{t+1}) are estimated from M_{t-1}, M_t, and M_{t+1}, respectively. The LSTM model then is trained to learn the temporal changing pattens from the image sequence of SR_{t-1} and SR_{t+1} to estimate SR_t. With the trained LSTM, the fusion image on date t can be generated using the HLS image sequence of H_{t-1} and H_{t+1}.

The structures of the SRCNN and LSTM models are shown in Fig. 5. Specifically, the SRCNN model consists of three convolutional components: feature extraction, non-linear mapping, and reconstruction. The feature extraction component is a convolutional operation that learns critical features from MODIS images and outputs the first hidden layer, namely the MODIS feature maps. The non-linear mapping component maps the spatial features of MODIS data to corresponding features in HLS and outputs the HLS feature maps. During this process, the sensor-induced reflectance difference can also be accommodated. The reconstruction component recovers the spatial details in the MODIS images and reconstructs the SR images at the HLS scale. The LSTM model employs two LSTM layers, each consisting of 100 LSTM cells to learn the temporal evolving patterns from the image sequence for fusion image prediction. LSTM cells encompass cell states and gating structures (i.e., input gates, forget gates, and output gates) to control the learning process. With the regulation of these gates, the memory information stored in the cell state is selectively preserved or discarded over time. The hyperparameters (e.g., number and size of convolutional filters) of SRCNN and LSTM are set in reference to our previous study (Yang et al., 2021), and the model parameters (e.g., weights and biases) are optimized to minimize the loss using the Adam method, which has an adaptive learning rate and can balance between the computational cost and training accuracy. The loss function of the model is the mean square

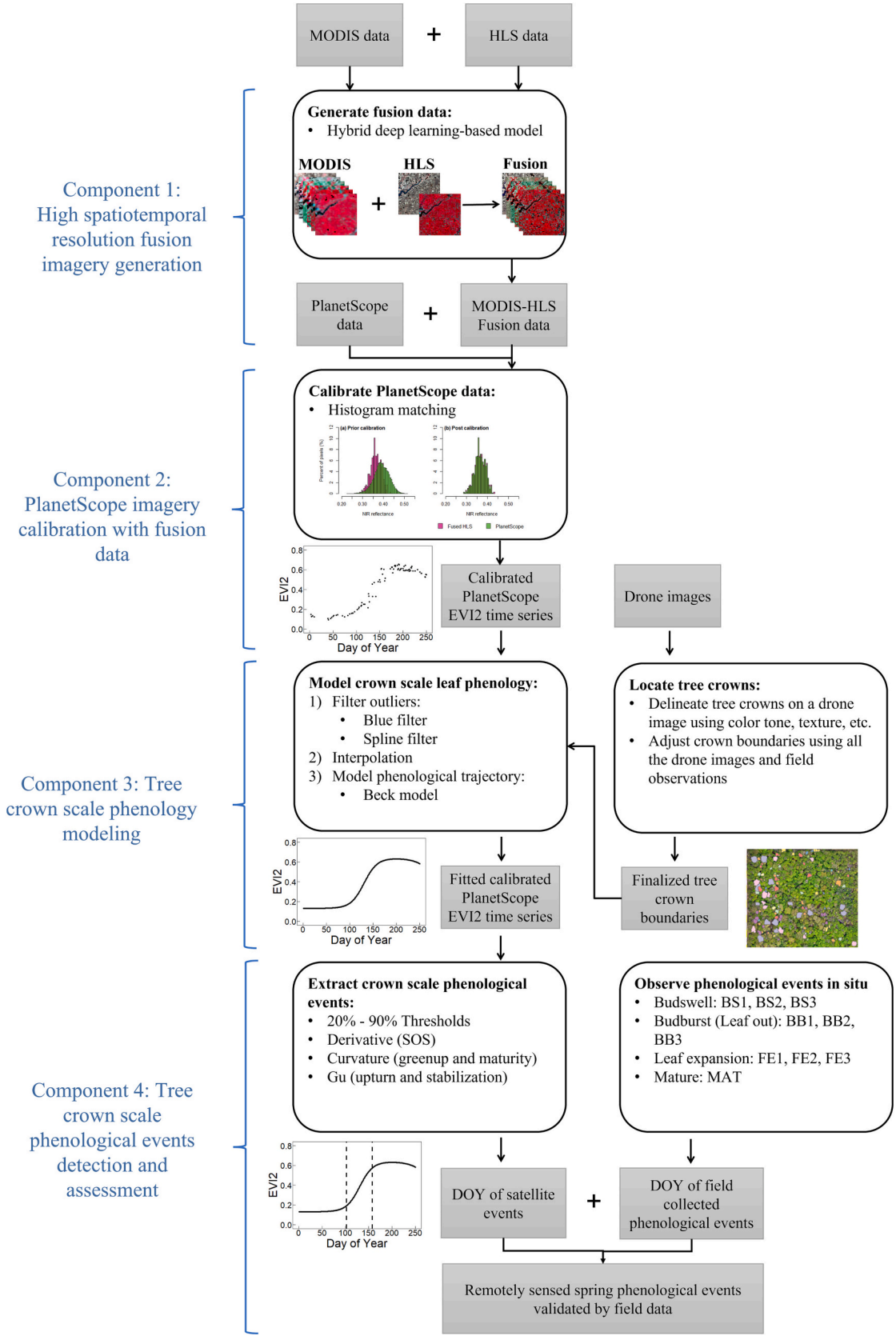

Fig. 3. The tree-crown scale remote sensing phenological monitoring framework to characterize all critical spring phenological events of individual trees in the fragmented forest setting.

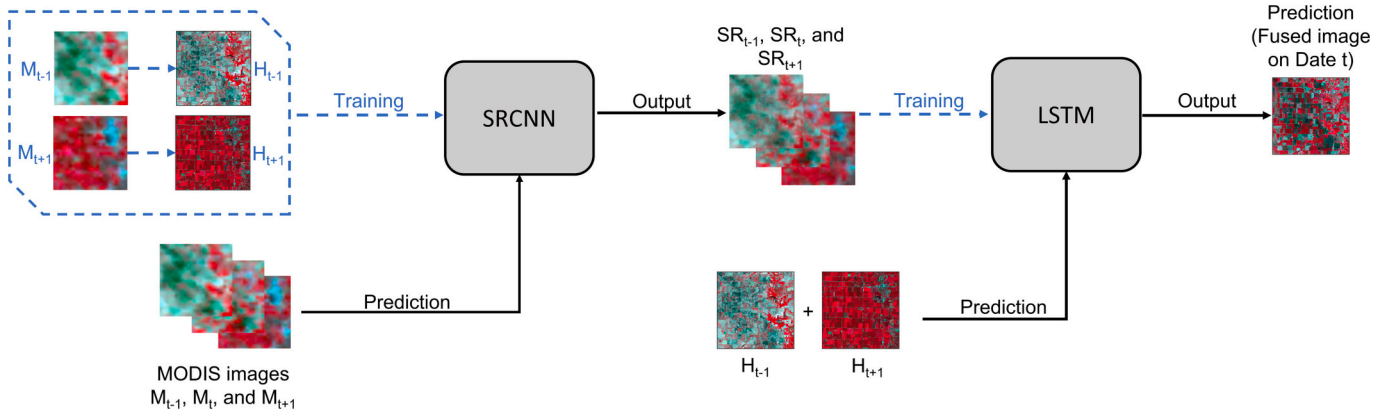

Fig. 4. The workflow of the hybrid deep learning model with the integration of SRCNN and LSTM. The training components of the model are represented with blue dashed arrows or boxes, while the prediction components are represented with black solid arrows. (For interpretation of the references to color in this figure legend, the reader is referred to the web version of this article.)

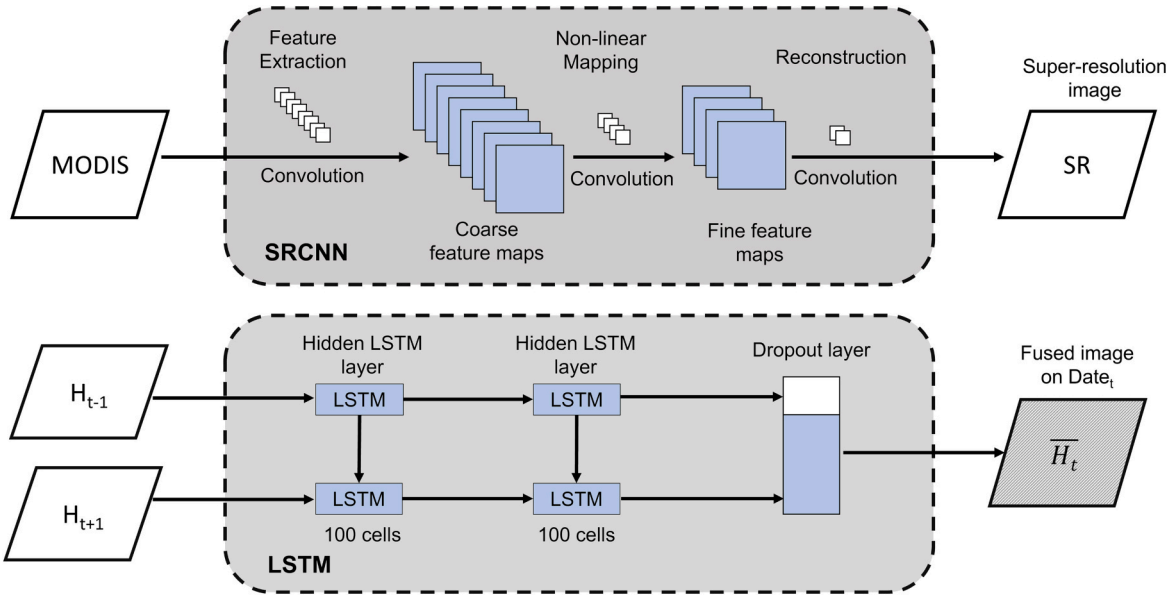

Fig. 5. The structures of SRCNN and LSTM models.

error between the predicted and reference reflectance values of the training samples. The hybrid deep learning model is built up using Keras with a TensorFlow backend in Python. Both the SRCNN and LSTM are trained for 100 epochs to converge. Each epoch for the SRCNN and LSTM model costs about 3 s and 35 s, respectively, using the NVIDIA GK110 "Kepler" K20X GPU accelerator. More information about the structure and parameters of the hybrid deep learning model can be found in our previous study (Yang et al., 2021). With the hybrid deep learning model, we generate the daily 30-m fusion imagery of the study site from DOY 1–250 for the years 2017–2020.

3.2. Calibration of PlanetScope imagery

Though the PlanetScope surface reflectance data have been atmospherically corrected, the additional calibration of PlanetScope imagery is needed due to cross-sensor radiometric inconsistency (Planet Labs, 2020). In spite of high spatial and temporal resolutions, the radiometric quality of PlanetScope data is not equivalent to that of rigorously calibrated conventional satellites (e.g., HLS and MODIS) (Houborg and McCabe, 2018). The satellites of PlanetScope have different orbital configurations and spectral response functions, leading to variations and inconsistency in radiometric quality of PlanetScope data. Besides, the PlanetScope surface reflectance data, despite rigorous geometric and atmospheric correction, are still subject to the BRDF effect (Planet Labs, 2020). The BRDF effect associated with sun-sensor geometry has been found to affect satellite-based leaf phenology monitoring (Galvão et al., 2011; Morton et al., 2014; Saleska et al., 2016). The PlanetScope imagery is acquired by the satellites with varying illumination geometry (i.e., sun azimuth and elevation), giving rise to noisy and biased reflectance values across sensors throughout the season. The cross-sensor radiometric calibration can be conducted via the use of pseudo-invariant spectral features to build linear transformations of spectral data between images, or via the use of high quality reference data (e.g., coarser resolution HLS and MODIS) to normalize the PlanetScope images of same acquisition dates (Frazier and Hemingway, 2021; Houborg and McCabe, 2018). As a reference-based calibration method, histogram transformation does not rely on identification of spectral invariant features and can be utilized to calibrate multi-satellite data into a consistent standard for enhanced sensor interoperability, and is thus adopted in this study.

To reduce the radiometric inconsistency among the PlanetScope data, we calibrate all the PlanetScope data with the corresponding

MODIS-HLS fused data using histogram matching. As both HLS and MODIS data are BRDF normalized, the calibration will also substantially reduce the BRDF effect on the PlanetScope data. Considering the landscape fragmentation of the study site, the original PlanetScope data and the fused data first are subset to the entire Trelease Woods area. To ensure the quality of histogram matching, the original PlanetScope data are masked with the quality assurance layer and only clear pixels that are not contaminated by cloud, cloud shadow, haze, and snow are included for the following analysis. Then the reflectance histograms of the Blue, Green, Red and NIR bands of masked original PlanetScope data are matched to the histograms of the corresponding bands of the MODIS-HLS fused data for each image acquisition date. Specifically, for each band, we obtain the cumulative distribution functions (CDFs) of both PlanetScope and fused data based on the reflectance histograms. We then calibrate the PlanetScope imagery by mapping its reflectance to the corresponding reflectance of the fused data of the same cumulative probability (Eq. 1).

$$y = cdf_f^{-1}\left(cdf_p(x)\right) \quad (1)$$

where, for each spectral band, y is the calibrated reflectance of the PlanetScope data, and x is the reflectance of the original PlanetScope data. cdf_f and cdf_p represent the CDFs of the fused data and the original PlanetScope data, respectively. The histogram matching is conducted using the Skimage package in Python. By calibrating the PlanetScope data with the same reference (i.e., MODIS-HLS fusion data), this histogram matching process largely resolves the issue of radiometric inconsistency across the sensors of PlanetScope constellation. With more consistent cross-sensor reflectance, the calibrated PlanetScope imagery is utilized for the subsequent tree-crown scale phenology modeling and event extraction.

To further demonstrate the role of the MODIS-HLS fusion data in calibrating the PlanetScope data of our fragmented forest site, we also calibrate the masked PlanetScope data to the daily temporal resolution MODIS MCD43A4 data using histogram matching for each image acquisition date. Despite the daily temporal resolution of the MODIS data, the 500-m spatial resolution makes the size of a MODIS pixel larger than the area of our study site. We thus consider the 10-km × 10-km study site-centered area for generating the reflectance histograms for both MODIS and PlanetScope data. To eliminate the influence of dramatically different reflectance of urban impervious surface, an urban mask is applied to remove urbanization areas. The reflectance of all masked original PlanetScope pixels located within the 10-km × 10-km area then is calibrated via the histogram matching using the corresponding MODIS reflectance data. The PlanetScope calibration results from the MODIS data then are compared to the calibration results from the MODIS-HLS fusion data of our study site for all the years (2017–2020).

3.3. Delineation of tree-crown boundaries

The tree-crown boundaries are delineated manually on the orthomosaic drone images with the assistant of field observations and field-collected GPS location of each tree crown (Fig. 6). To delineate the tree crowns, we first refer to the drone image collected on October 25 in 2018, because that image has a more distinct color tone difference among tree crowns during the fall coloration period. For those tree crowns (e.g., clumping or touching tree crowns) that are difficult to identify on this drone image due to the delayed leaf coloration timing, we further leverage the orthomosaic drone images on October 11 and November 2, 2018, as well as the images on May 6, June 2, September 17, and November 4 in 2019 for the crown boundary delineation and adjustment. The drone images collected on multiple dates across seasons document the tree phenological progress and leaf color change. Given the intra- and inter-specific variation in tree phenology, these drone images largely facilitate the identification of the 123 tree crowns and delineation of corresponding crown boundaries. To delineate a tree crown's boundary, we mainly leverage the tree color tone, texture, spatial structure, morphology, as well as tree field measures (e.g., tree diameter at breast height [DBH] and basal area) and field observations (e.g., tree phenological stages on the drone imagery acquisition dates). Tree crowns are first located based on the GPS information as well as the tree morphology and field phenological observations. The adjoining drone image pixels that maintain similar color tone and texture then are grouped into the same tree crown. Different tree crowns are usually separated by a 'gap', where understory or ground is exposed, especially in the drone images collected in autumn. The sizes and boundaries of tree crowns are further adjusted with consideration of tree species' field measures, such as basal area, particularly for clumping and touching crowns. The manual delineation process of the 123 tree crown boundaries with consideration of a diverse set of tree characteristics is crucial for locating accurately individual trees on the PlanetScope imagery across crown sizes, which otherwise may be compromised by more automatic image segmentation methods.

3.4. Model tree-crown scale phenology and retrieve satellite events

For each individual tree with field-collected phenological data, the median EVI2 of all the pixels located totally within the crown boundary is calculated from each calibrated PlanetScope image to generate the time series for phenological modeling. As a widely used vegetation index, EVI2 is selected in this study owing to its reduced sensitivity to the noise of the blue band which is more subject to the influence of atmospheric interference (Jiang et al., 2008). EVI2 is also functionally equivalent to EVI which can eliminate atmospheric and canopy background noises, as well as remain sensitive to canopy change when leaf area index is high (Huete et al., 2002; Reed et al., 2009). The EVI2 time series first is pre-processed using the night and spline filters to reduce the influence of sensing noises and outliers. With the night filter, the PlanetScope observations collected under scarce illumination conditions with abnormally low EVI2 values are removed. The spline filter, based on recursive spline smoothing and residual computation, removes the outliers falling outside a defined residual envelope. Specifically, we fit the cubic smoothing spline to the EVI2 time series, with the residuals calculated between fitted and observed values. The observations with

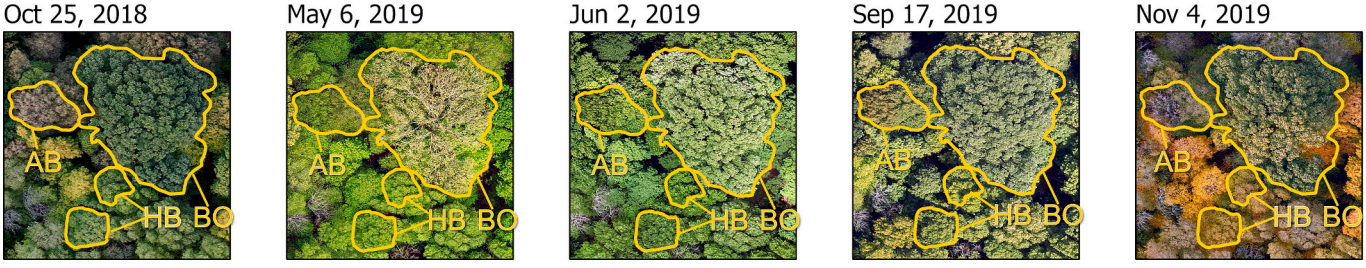

Fig. 6. Tree crown boundary of one *Q. macrocarpa* (BO), one *T. americana* (AB), and two *C. occidentalis* (HB) in five drone images. The color tone difference of tree crowns on different dates aids the crown delineation and adjustment.

the residuals outside the envelope of μ ± 3σ (μ and σ represent the mean and standard deviation of the residuals, respectively) are taken as outliers and thus are removed. This spline smoothing and outlier removal process is repeated until no outliers are detected with this filter. After removing the abnormal observations, we then fill in the missing values of the EVI2 time series using linear interpolation.

With the pre-processed EVI2 time series, we employ the Beck logistic-based phenological curve fitting function to model the leaf phenological development of tree crowns during the spring season (Eq. (2)) (Beck et al., 2006).

$$f(t) = mn + (mx - mn) \bullet \frac{1}{1 + e^{(-rsp*(t-S))}} \quad (2)$$

Here, $f(t)$ is the logistic-fitted EVI2 value at time *t*. *mn* and *mx* represent the off-season EVI2 value and maximum EVI2 value, respectively. *S* denotes the inflection point of the fitted curve in spring and rsp is the rate of increase of the fitted curve at the inflection point *S*. The off-season is defined as the plant dormant period before the season starts in the study site, and the off-season EVI2 value is calculated as the median EVI2 of clear observations during this period. The observation values lower than the off-season EVI2 then are replaced with the off-season EVI2 to mitigate the impact of spurious observations, particularly caused by snow and ice, similar to Beck et al. (2006). The other parameters are estimated using the iterative non-linear least square optimization method.

The logistic-based phenological curve fitting function has been widely utilized to model plant seasonal phenological dynamics under varying environmental conditions. It has been found to outperform several other phenological curve fitting functions (e.g., asymmetric Gaussian function and polynomial function) in monitoring phenological change of deciduous forests (Berra and Gaulton, 2021; Zhang et al., 2003; Zhu et al., 2011). The logistic-based function can capture abrupt changes in the EVI2 time series at the beginning of the season, and is also advantageous with the phenological implications of its function parameters (e.g., *mn, mx, rsp,* and *S*) and function flexibility to adapt to a range of plant growth scenarios (Beck et al., 2006; Diao, 2020; Diao and Li, 2022).

With the logistic-fitted phenological curve, four phenological metric extraction methods, namely derivative-based, curvature-based, Gu-based, and threshold-based methods, are employed to retrieve phenological metrics of various satellite events (Beck et al., 2006; Gu et al., 2009; Klosterman et al., 2014; White et al., 1997). Specifically, the derivative-based method is utilized to extract the start of season (SOS) satellite event via the local maximum of the curve first derivative during the spring season. The curvature-based method is used to extract two satellite events (i.e., greenup and maturity) via the rate of change in curvature during spring. The greenup and maturity satellite events correspond to the timing of first and second local maxima of the curvature change rate, respectively. As regards the Gu-based method, two satellite events (i.e., upturn and stabilization) are retrieved via the intersections of the recovery line and the boundary lines (i.e., baseline and maxline). The recovery line is the line tangent to the fitted curve at the point of the curve maximum first derivative. The baseline and maxline are the horizontal lines of the off-season EVI2 and maximum EVI2, respectively. The upturn satellite event corresponds to the timing of the intersection between the recovery line and the baseline, while the stabilization event corresponds to the timing of the intersection between the recovery line and the maxline. In total, we extract five curve feature-based satellite events (i.e., SOS, greenup, maturity, upturn, and stabilization). These diverse set of events characterize the timing of phenological changes in terms of leaf biophysical and biochemical content with distinct curve properties (Berra and Gaulton, 2021; Filippa et al., 2016; Zeng et al., 2020).

Besides the curve feature-based methods, we also employ the threshold-based method to extract satellite events via the percent of EVI2 amplitude. Specifically, the percent thresholds ranging from 10% to 90% with an interval of 10% are utilized to extract a multitude of threshold-based satellite events during the spring season. The phenological curve fitting and phenological metric extraction processes are conducted in R with Phenopix and Greenbrown packages.

3.5. Accuracy assessment

For the MODIS-HLS fusion images generated with the hybrid deep learning model, we evaluate the fusion results using the root-mean-square-error (RMSE) of each band, erreur relative global adimensionnelle de synthese (ERGAS) and spectral angle mapper (SAM) (Chaithra et al., 2018). ERGAS, in terms of the normalized RMSE across bands, measures the spectral difference between the fused and reference HLS images (Eq. 3). ERGAS takes into account the differences in the reflectance values across bands and the extent of the resolution difference between HLS and MODIS images. A lower ERGAS value indicates that the fused image is more similar to the reference image (i.e., HLS image).

$$ERGAS = 100\frac{h}{l}\sqrt{\sum_{b=1}^{M}\left[\frac{RMSE(\widehat{L}_b)^2}{\mu_b}\right]} \quad (3)$$

Here, h and l are the spatial resolutions of HLS and MODIS images, respectively; M is the number of bands. As Red and NIR bands are utilized for calculating EVI2, M is equal to 2 in this study. $\widehat{L}_b$ denotes the estimated reflectance value of band *b*, while μ_b represents the mean reflectance of band *b*.

SAM measures the spectral similarity between the fused image and the reference HLS image across bands (Eq. 4). For each pixel, the spectral reflectance information can be denoted as an N-dimensional spectral vector, where N equals the number of bands. SAM can be calculated as the mean of angles between the estimated and reference spectral reflectance of all pixels in the N-dimensional space. A smaller SAM value indicates that the spectral distortion is lower in the fused image.

$$SAM = \frac{1}{N}\sum_{n=1}^{N} arccos\frac{\sum_{b=1}^{M}\left(\widehat{L}_n^b L_n^b\right)}{\sqrt{\sum_{b=1}^{M}\left(\widehat{L}_n^b\right)^2\sum_{b=1}^{M}\left(L_n^b\right)^2}} \quad (4)$$

where, N denotes the number of pixels in the fused or reference image. $\widehat{L}_n^b$ and L_n^b represent the spectral reflectance of pixel n in band b of the fused and reference images, respectively.

The dates of satellite events extracted from the calibrated PlanetScope data are validated with those of the field events. Specifically, the coefficients of determination (R^2), *p*-value of coefficients, bias, and RMSE are calculated between the DOY of each field event and the DOY of corresponding relevant satellite events. The R^2, p-value of coefficients, bias, and RMSE denote the proportion of the variation in the DOY of field events explained by that of corresponding satellite events, as well as the significance of the regression coefficient, the mean DOY difference, and the extent of DOY difference between the timing of field and satellite events, respectively.

To further explore the effect of tree-crown size on the accuracy of spring phenological events detection, the differences in DOYs between the field events and corresponding satellite events are calculated for all 123 trees. Then, the DOY differences between field and satellite events are aggregated by species and year, and are analyzed across tree-crown sizes at the species level.

4. Results

4.1. Tree-crown area distribution

The boundary of a tree crown is delineated based on the drone imagery collected in 2018 and 2019 and its crown area is calculated from the manually delineated tree-crown boundary in ArcGIS Pro. The area of

tree crowns ranges from 7.6 to 431.6 m^2, with an average of 112.8 m^2. Among species, *Q. macrocarpa* (BO) has the largest tree crown area (305.7 ± 81.6 m^2) (mean ± 1 SD) and *U. rubra* (SE) has the smallest area (42.0 ± 1.3 m^2). Large variation in crown sizes also exists among individuals within a species. The greatest variation in intraspecific sizes is in *Q. rubra* (RO) (233.5 ± 87.9 m^2). Individuals with tree crown sizes >90m^2 (usually covering ≥10 calibrated PlanetScope pixels) are designated as 'large individuals'; these individuals are mostly from dominant species of Trelease Woods. In total 42% of the 123 individual trees exceed the 90-m^2 threshold of large trees (Fig. 7 (a)). With this threshold, the large trees include almost all individuals of *Q. macrocarpa* (BO) and *Q. rubra* (RO), two original dominant tree species, and some individuals of *Acer saccharum* (SM), *Carya laciniosa* (SH), and *Celtis occidentalis* (HB) – the more recent dominant species (Fig. 7 (b)). The selected threshold successfully differentiates small trees from large trees, both interspecifically and intraspecifically, and helps include a large enough number of pixels to ensure that the median EVI2 of each crown is robust to extreme values.

4.2. Field-collected phenological events

With field phenological observations, we summarize the timing for 10 field phenological events of five species using corresponding large individuals from 2017 to 2020 (Fig. 8 and Table S1). All species have contrasting phenology timing among the four years (Fig. 8) and the significance of interannual differences for 10 field phenological events of all five species is further evaluated using Analysis of Variance (ANOVA) (Table S2). For all the tree species, the interannual differences are statistically (or marginally) significant for most phenological events. Across years, the species tend to enter all the phenophases relatively early in 2017, but have delayed timing in 2018 for budswell and budburst phases, and in 2020 for leaf expansion and mature phases. For each year, we also test the significance of interspecific differences for 10 field phenological events using ANOVA, and the interspecific differences for almost all the events are statistically significant (Table S3). The three budswell events, three budburst events, and leaf expansion 1 and 2 phenological events have the largest interspecific differences in 2020 and smallest differences in 2018 (Fig. S1). The leaf expansion 3 and mature events also have the largest interspecific differences in 2020, yet with similar levels of interspecific differences for the other three years. The species exhibit diverse and heterogenous inter-annual patterns for the field phenological events across phenophases. Among the species, *A. saccharum* tends to reach all the phenophases relatively early during the study period, while *C. laciniosa* has relatively delayed timing for most phenological events. The intraspecific differences for 10 field phenological events of each species are not statistically significant using ANOVA (Table S4).

Given the comparable inter- and intra-specific patterns of field phenological events within a phenological phase, we focus mainly on six field phenological events, namely BS1, BB1, BB3, FE1, FE3, and MAT, throughout the spring leaf phenological development trajectory in this study. These six field events represent the most critical phenological events from initial budswell to final mature phases.

4.3. Fusion of MODIS and HLS data

In total, 250 fused images from DOY 1–250 are generated for each year to facilitate subsequent phenological trajectory modeling and phenological events detection. Fig. 9 shows the examples of the Trelease Woods region of the MODIS, HLS, and corresponding predicted fusion images in spring across four years (i.e., DOY 162 in 2017, DOY 117 in 2018, DOY 161 in 2019, and DOY 166 in 2020). We compare the spatial patterns of color tone, texture, and land cover of predicted images (Fig. 9 (c)) with those of the reference images (Fig. 9(b)). The fused images do capture well the rapid change of reflectance in MODIS images and preserve the spatial characteristics of HLS images, particularly for the fragmented forest. The overall color tone, texture, and distribution of agricultural fields, vegetated areas, urban regions, and waterbodies in fused images are similar to those in corresponding HLS images. While images are generally cloud-free with proportions of contaminated pixels <10%, a small number of pixels in the HLS images are masked out due to cloud contamination or other noises, shown as the small black squares in Fig. 9 (b and c).

ERGAS (Red and NIR bands), SAM (Red and NIR bands), RMSE of the Red band, and RMSE of the NIR band are selected as the accuracy metrics to assess the fusion model performance. The accuracy metrics are calculated based on the reference masked HLS and corresponding fusion images before DOY 200, as all trees observed in this study reach the mature phenophase before DOY 200 in all four years. Only the pixels with valid values in both HLS and fused images are included for accuracy assessment. Table 4 shows the mean and standard deviation of ERGAS, SAM, RMSEs of the red and NIR bands across years, using all the reference HLS images (i.e., images of DOY 66, 130, 162 and 178 in 2017, DOY 101 and 117 in 2018, DOY 56, 161, and 176 in 2019, and DOY 1, 123, 166, and 187 in 2020). The mean RMSE values for the Red and NIR bands are mostly lower than 0.02, except for RMSE of NIR in 2017 (0.026) (Table 4). The mean ERGAS values range from 0.4 to 0.846, and the mean SAM values are around 0.030 for all four years. The ERGAS and SAM values also are low in comparison with existing literature (Yang et al., 2021). Among the four years, 2017 and 2020 have slightly

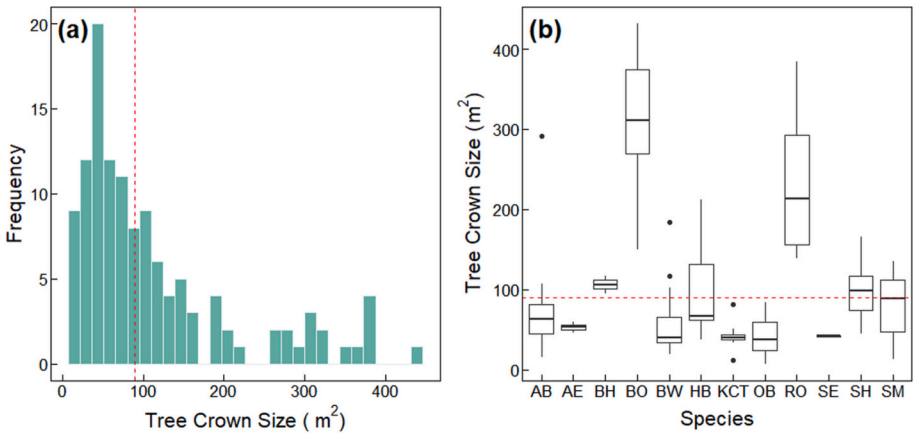

Fig. 7. Area distribution of tree crowns in Trelease Woods. (a) Histogram of crown areas across all 123 trees. (b) Tree crown area boxplot for each of 12 study species. The red dashed line indicates the 90m^2 threshold separating large and small trees. Tree abbreviations are in Table 1. (For interpretation of the references to color in this figure legend, the reader is referred to the web version of this article.)

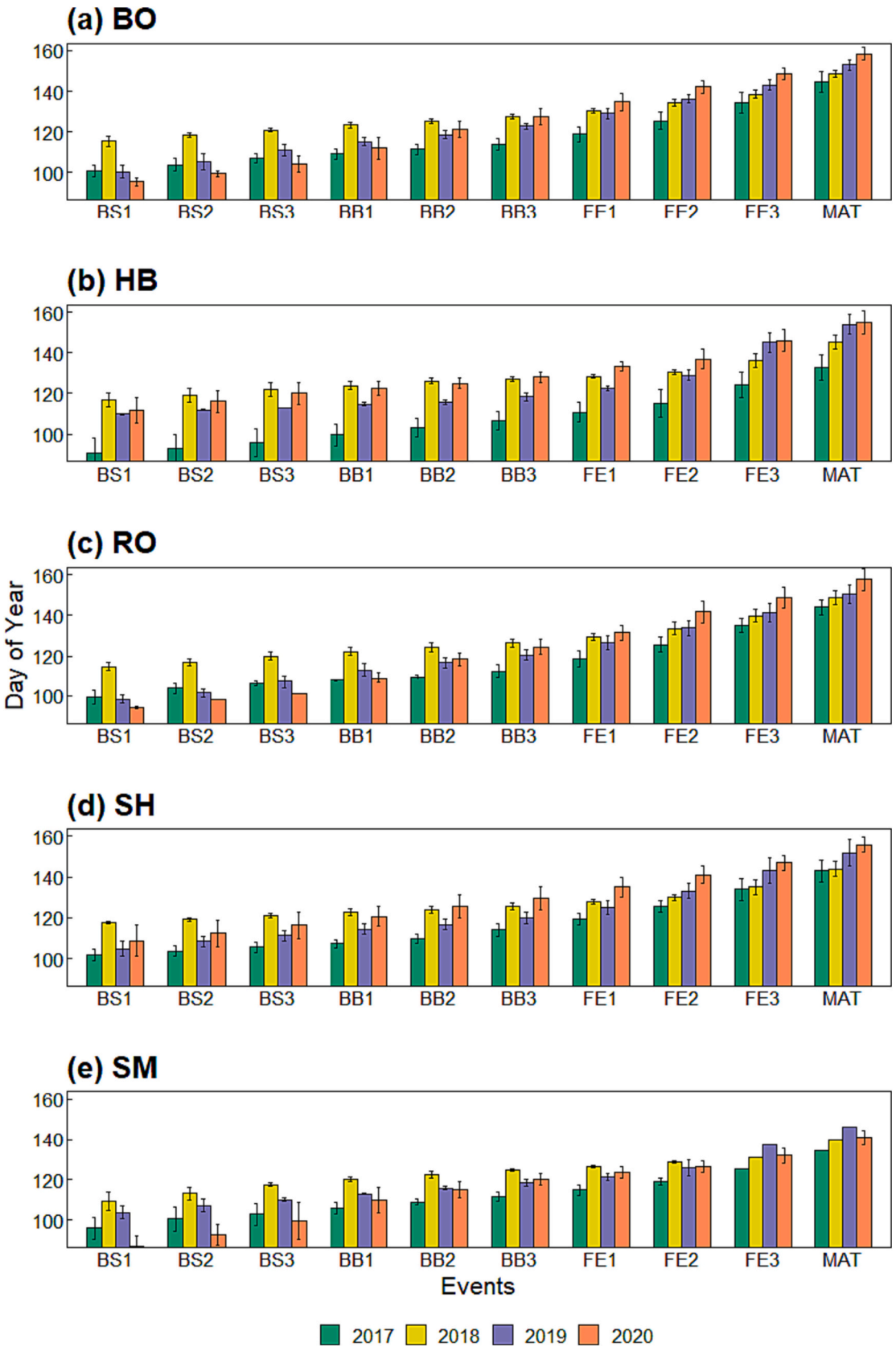

Fig. 8. Interannual variation of the dates (mean ± SD) of ten field-collected phenological events for the large individuals of five species (BO – *Q. macrocarpa,* HB – *C. occidentalis,* RO – *Q. rubra,* SH – *C. laciniosa,* SM - *A. saccharum*) from 2017 to 2020.

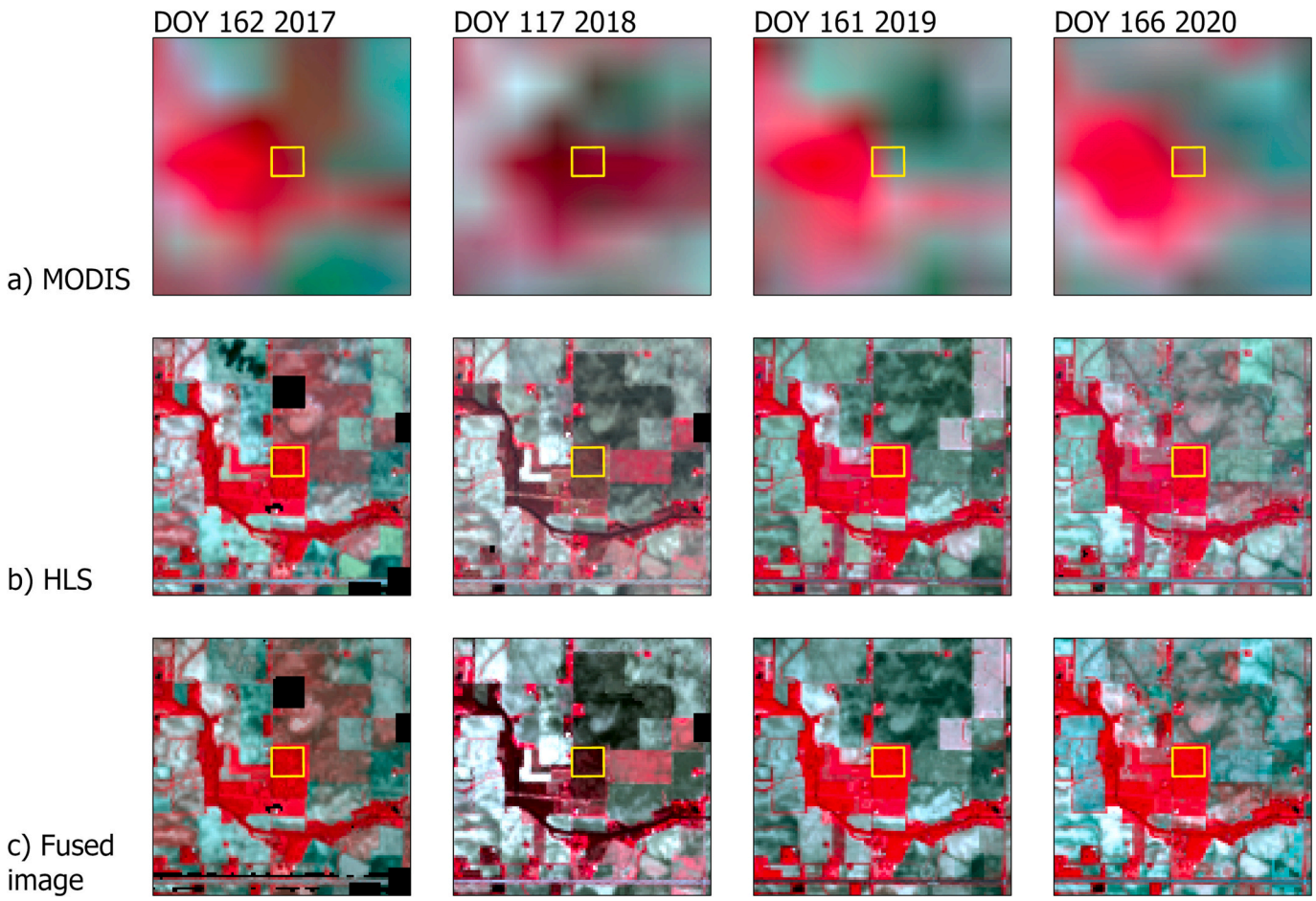

Fig. 9. The comparison of resampled MODIS images (a), masked HLS images (b), and fused images (c) of DOY 162 in 2017, DOY 117 in 2018, DOY 161 in 2019, and DOY 166 in 2020. The yellow solid square in each image represents the study site (i.e., north half of Trelease Woods). (For interpretation of the references to color in this figure legend, the reader is referred to the web version of this article.)

Table 4
Mean and standard deviation of accuracy metrics SAM, ERGAS, and RMSE of Red or NIR bands for fused images before DOY 200 from 2017 to 2020.

Year	RMSE of Red	RMSE of NIR	ERGAS (2 band)	SAM (2 Band)
2017	0.014 ± 0.008	0.026 ± 0.014	0.846 ± 0.570	0.031 ± 0.005
2018	0.007 ± 0.001	0.013 ± 0.002	0.400 ± 0.049	0.032 ± 0.001
2019	0.009 ± 0.002	0.012 ± 0.004	0.454 ± 0.061	0.032 ± 0.007
2020	0.012 ± 0.008	0.022 ± 0.015	0.763 ± 0.482	0.030 ± 0.011

higher RMSE and ERGAS values compared to the other two years, which possibly may be due to the temporal distribution of available dates and cloud contamination. Overall, all accuracy metrics suggest high agreement between the fused images and the reference HLS images.

4.4. Histogram matching of original PlanetScope data

The histogram of the Blue, Green, Red or NIR band of all original PlanetScope pixels located within the entire area of Trelease Woods is matched to the reflectance histogram of the corresponding band of fused data located within the same area. To examine the performance of histogram matching, we first compare the reflectance histograms of the red (or NIR) band prior- and post-calibration (Fig. 10 as an example). After histogram matching, the mean and standard deviation of calibrated PlanetScope histogram are closer to those of the corresponding fusion histogram. Compared to the original PlanetScope band histogram, the shape (i.e., width, peak, and value distribution) of the calibrated PlanetScope band histogram is more comparable to that of the fusion band histogram.

The mean and standard deviation of EVI2 time series of both uncalibrated and calibrated PlanetScope images for the study site are shown further in Fig. 11. The uncalibrated EVI2 values across PlanetScope images show more variation and fluctuation compared to calibrated ones. Upon comparison with the fused images, the mean EVI2 (gray points in Fig. 11) of calibrated PlanetScope data with histogram matching is closer to that of fused data, with improved radiometric consistency across the images. The standard deviation of EVI2 time series also decreases after the PlanetScope imagery calibration. Using mean EVI2 of fused images as reference, the RMSE of original PlanetScope mean EVI2 (RMSE from 0.045 to 0.065) is larger than that of the corresponding calibrated PlanetScope mean EVI2 (RMSE <0.01) for four years. After the calibration with histogram matching, the radiometric inconsistency across the PlanetScope data has largely been reduced. The histogram matching also decreases the fluctuation of PlanetScope data during the off-season (DOY 1–100) and near-peak greenness period (DOY 150–250). In general, the histogram matching calibration adjusts the reflectance of PlanetScope data with reference to the fused data, decreases the reflectance difference across PlanetScope images, and generates smoother time series for further phenological trajectory modeling and phenological events detection.

We also evaluate the feasibility of calibrating the PlanetScope images to the corresponding MODIS images using histogram matching (Fig. 12). In general, this MODIS-based calibration also can adjust the distribution of reflectance of the original PlanetScope data, but the EVI2 time series

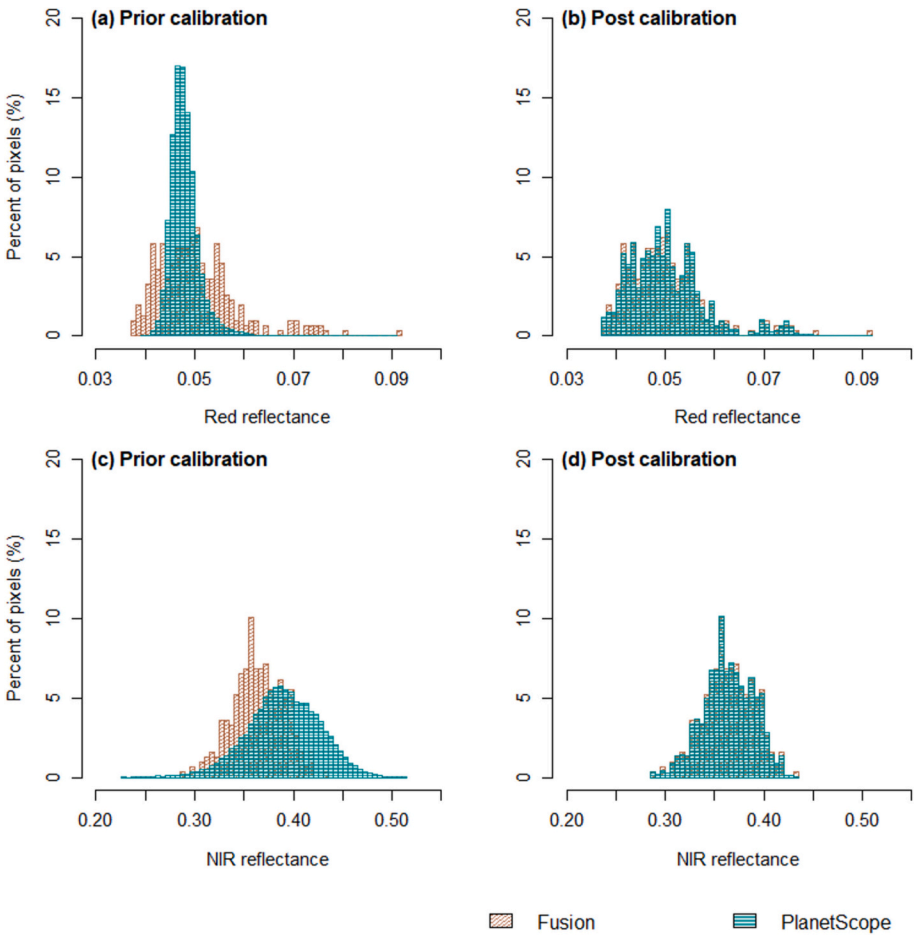

Fig. 10. Example histograms of Red and NIR bands of original PlanetScope data, calibrated PlanetScope data, and fusion data on May 31, 2020. (For interpretation of the references to color in this figure legend, the reader is referred to the web version of this article.)

of the PlanetScope data calibrated to MODIS data (hereafter 'Planet – MODIS') is not appropriate for the following phenological events detection and assessment process. The mean EVI2 time series of Planet – MODIS in the study site is more comparable to that of surrounding agriculture with delayed plant growth and shorter growing season (Fig. 12). As our fragmented forest site (area less than that of one MODIS pixel) is located in a mixed landscape, the cumulative histogram of reference MODIS data used for calibrating original PlanetScope data is constructed based on the reflectance mixture of Trelease Woods and surrounding land covers. The portion of the forest pixels is small in the reflectance histogram, which makes it difficult to characterize the patterns of the histogram via forest pixels. The limited number of forest pixels thus brings more uncertainties in histogram matching, leading to a higher fluctuation in the EVI2 time series of the Planet – MODIS data. The RMSE between the mean EVI2 of Planet – MODIS and that of fused data ranges from 0.057 to 0.099, much larger than the RMSE between the corresponding mean EVI2 of Planet – Fused HLS and that of fused data. Because of the large area of agriculture, the EVI2 time series of Planet – MODIS has a different shape from that of forest, indicating the potential issue with MODIS as the calibration reference. The histogram matching of PlanetScope to the fused HLS data is thus employed for the subsequent analysis.

4.5. *Bridge satellite events to field phenological events for large trees*

For each large individual, the EVI2 time series of calibrated PlanetScope data each year is fitted using the Beck model. The mean and standard deviation of RMSE between fitted and calibrated EVI2 of all large individuals are summarized in Table S5. The relatively small RMSE (mean RMSE ranging from 0.03 to 0.06) indicates the feasibility of modeling a tree's phenological trajectory using the Beck.

With BS1, BB1, BB3, FE1, FE3, and MAT as the target field events, each of these events is compared with all the satellite-based phenological events (i.e., threshold 10% to 90%; derivative-based SOS; curvature-based greenup and maturity; Gu-based upturn and stabilization) for each large individual in the study site. The comparative analysis is summarized per species (with >5 large individuals) and year with accuracy metrics calculated (i.e., RMSE, R^2, and bias) (Fig. 13). For each target field event, the corresponding satellite event then is identified using the lowest RMSE with all the considered large individuals. In general, all target field events of large individuals tend to be more accurately estimated using the threshold-based method, possibly due to the comprehensive thresholds covering the tree spring phenological development trajectory considered in this study (Fig. 13). The dates of satellite events of large individuals extracted from calibrated PlanetScope data tend to be closer to the dates of corresponding field events compared to original PlanetScope data (Fig. 14).

With consideration of all satellite events, the field events BS1, BB1, BB3, FE1, FE3, and MAT can be approximated more accurately using the 20%, 30%, 40%, 50%, 70%, and 80% thresholds, respectively (Fig. 13 and Fig. 14). With the calibrated PlanetScope data, the mean field event timing aligns with the corresponding mean satellite event timing per species and year along the 1:1 line, with R^2 from 0.391 to 0.901, RMSE from 3.307 to 8.042 days, and bias from 1.564 to 4.272 days. Among the target field events, BB1, BB3, and FE1 can be identified with higher accuracy (i.e., higher R^2 and lower RMSE) by their corresponding

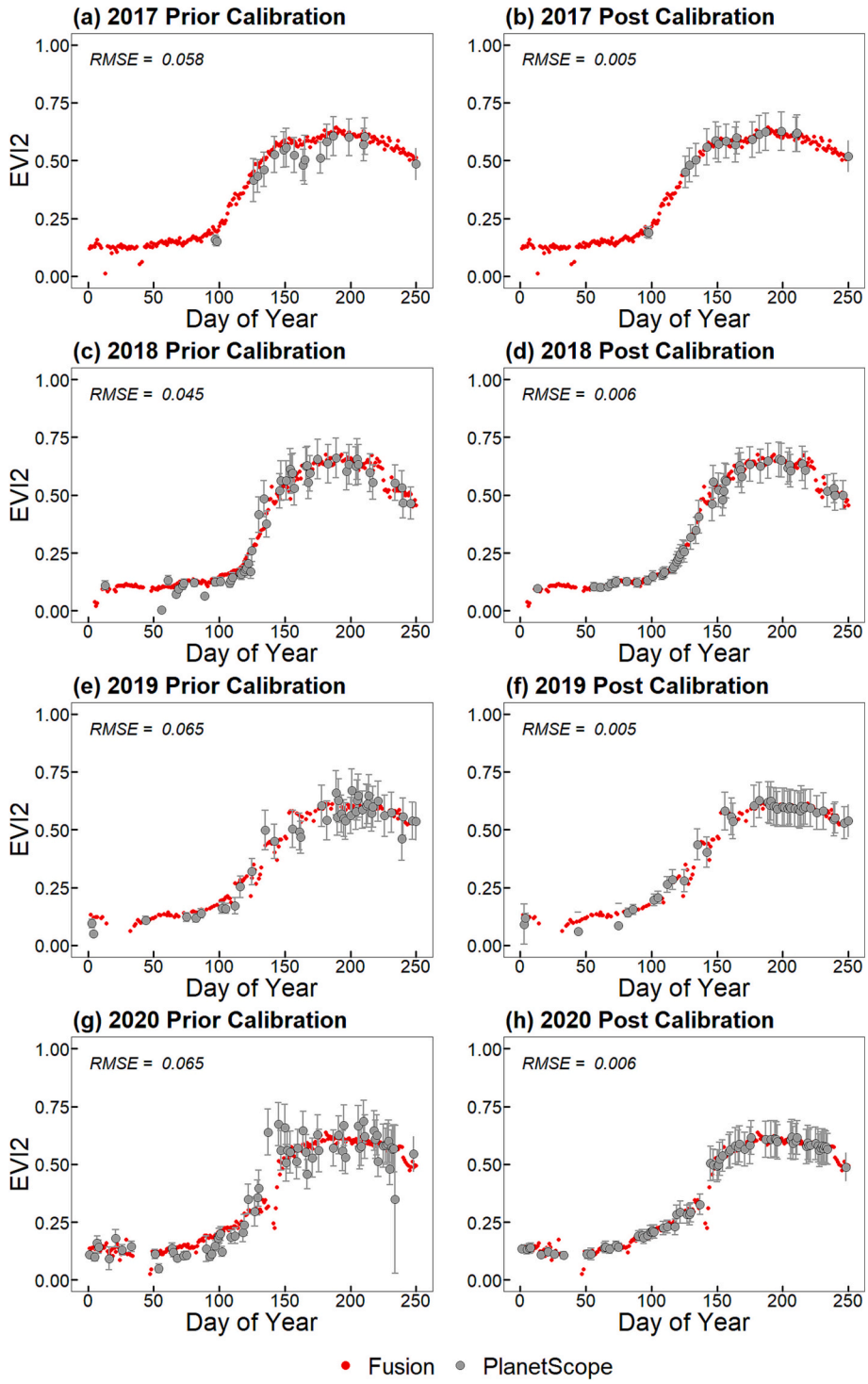

Fig. 11. Seasonal variation in EVI2 derived from original and calibrated PlanetScope data from 2017 to 2020. Vertical error bar represents one standard deviation among all pixels located in the north half of Trelease Woods. Red dots denote the corresponding mean EVI2 values of the fused data. (For interpretation of the references to color in this figure legend, the reader is referred to the web version of this article.)

thresholds using both calibrated and original PlanetScope data, representing the stronger potential of satellite imagery in detecting remotely the tree budburst, full leaf out, and early leaf expansion events in spring. Variation in the mean phenological timing of these field events can be captured well by that of corresponding satellite events. Particularly, the mean DOY of BB3 per species and year aligns closely with the corresponding mean DOY of threshold 40% of calibrated PlanetScope EVI2 time series, with R^2 of 0.901, RMSE of 3.307 days, and bias of 2.55 days (Fig. 13). The mean DOY of FE1 per species and year can be approximated by the corresponding mean DOY of calibrated EVI2 threshold 50% (R^2 being 0.81, RMSE being 5.03 days, and bias being 3.968 days). In the early spring, the weak signal of budswell is more difficult to be captured both in-situ and by the satellite imagery, and the detection of early field events (e.g., BS1) also may be subject to the influence of understory, soil background, and snow contamination. The detection accuracy of BS1 thus decreases with R^2 of 0.391, RMSE of 8.042 days,

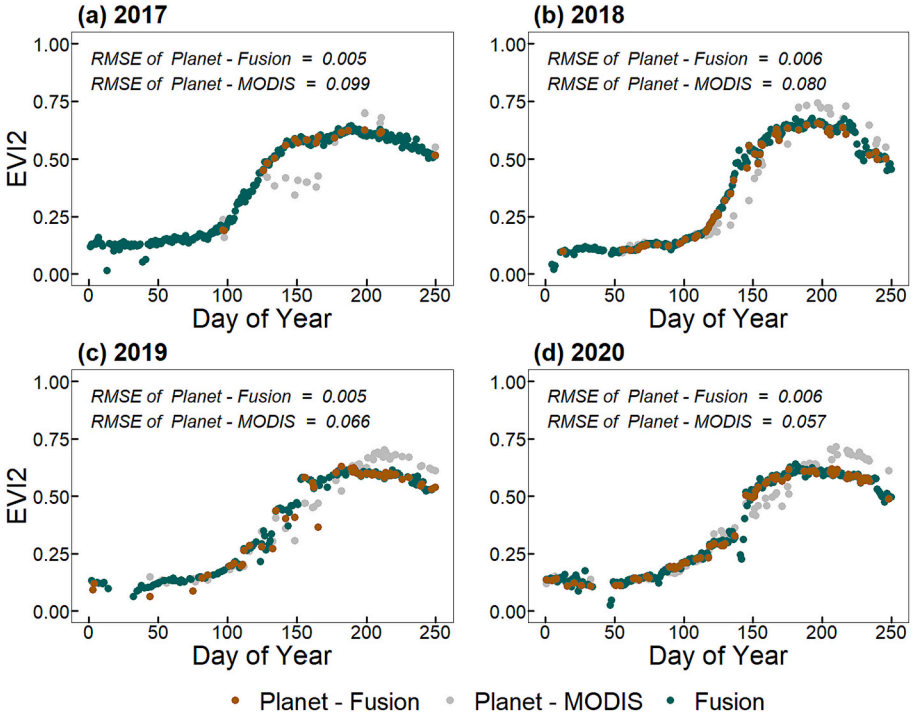

Fig. 12. Comparison of mean EVI2 time series curves from Planet – Fusion, Planet – MODIS, and fusion data, for 2017 to 2020, where Planet – Fusion represents PlanetScope data calibrated with fused images, and Planet – MODIS stands for the PlanetScope data calibrated with MODIS data.

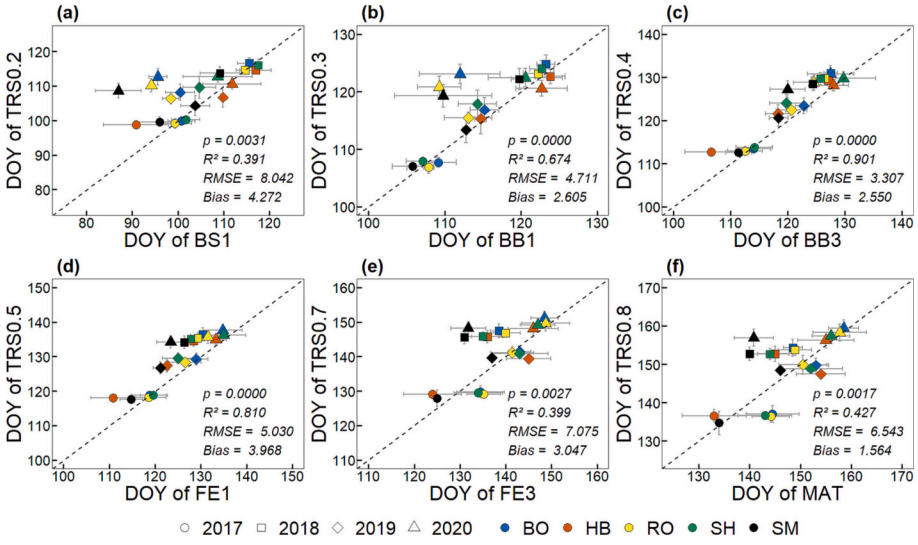

Fig. 13. The mean DOY of six field events (i.e., budswell 1, budburst 1, budburst 3, leaf expansion 1, leaf expansion 3, and mature) approximated by the mean DOY of corresponding satellite events (i.e., 20%, 30%, 40%, 50%, 70% and 80% thresholds [TRS]) per species and year using the calibrated PlanetScope data. Each field event is approximated by the satellite event with the lowest RMSE. Vertical and horizontal error bars represent one standard deviation of DOY of satellite events and field events, respectively. Species each have more than five large individuals, including BO – *Q. macrocarpa*, HB – *C. occidentalis*, RO – *Q. rubra*, SH – *C. laciniosa*, SM - *A. saccharum*.

and bias of 4.272 days. At the end of spring, the change of tree leaf status (e.g., from leaf expansion to maturity) is more subtle than that during the leaf out and early expansion phases, making it more difficult to detect FE3 and MAT events using satellite imagery. Accordingly, variation in the timing of these two field events across species is harder to characterize. Compared to original PlanetScope data, the calibrated data achieve higher R^2 for most field phenological events, indicating that more variation in field event timing across species and years can be explained by the corresponding satellite event with the calibration of PlanetScope imagery (Fig. 13 and Fig. 14).

With the increasing use of curve feature-based (i.e., derivative-, curvature-, and Gu-based) phenological metric extraction methods in phenological studies, we further evaluate the congruence between the satellite events from those methods with the corresponding field events. Specifically, each satellite event (e.g., derivative-based SOS) is compared with all field events for each large individual in the study site, and the field event with the lowest RMSE is selected based on the summarized comparative analysis per species (with >5 large individuals) and year (Fig. 15), similar to Fig. 13. The Gu-based upturn and curvature-based greenup events approximate the field event BS1, with RMSE around 7–9 days and R^2 around 0.45. These two satellite events are negatively biased, with overall estimates earlier than the beginning of tree budswell, possibly due to the earlier emergence of understory species. The derivative-based SOS event has good congruence with the field event FE2, achieving the R^2 of 0.591, RMSE of 5 days, and almost no bias. The Gu-based stabilization and curvature-based maturity events can be aligned with the field event MAT, yet positively biased with R^2 around 0.4 and RMSE over one week. The delayed

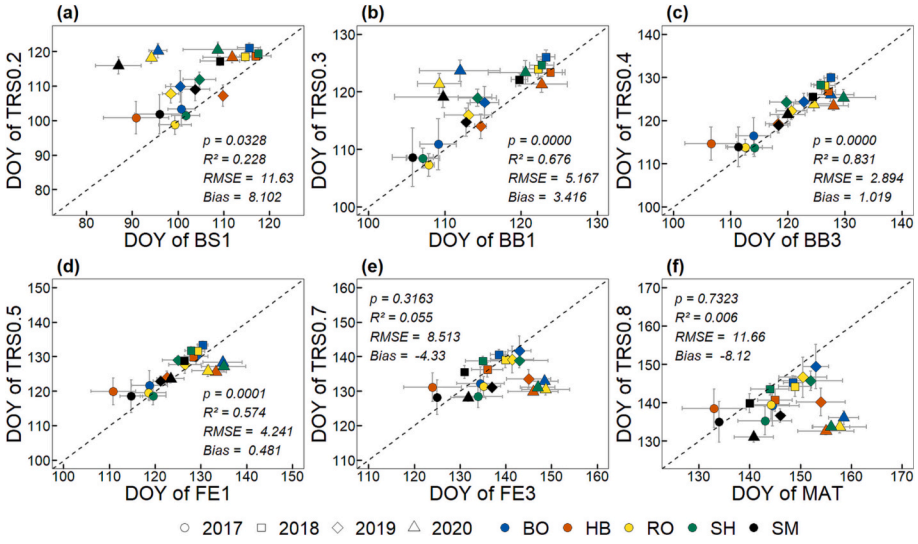

Fig. 14. The mean DOY of six field events (i.e., budswell 1, budburst 1, budburst 3, leaf expansion 1, leaf expansion 3, and mature) approximated by the mean DOY of corresponding satellite events (i.e., 20%, 30%, 40%, 50%, 70% and 80% thresholds [TRS]) per species and year using the original PlanetScope data. Each field event is approximated by the satellite event with the lowest RMSE. Vertical and horizontal error bars represent one standard deviation of DOY of satellite events and field events, respectively. Species each have >5 large individuals, including BO – *Q. macrocarpa*, HB – *C. occidentalis*, RO – *Q. rubra*, SH – *C. laciniosa*, SM - *A. saccharum*.

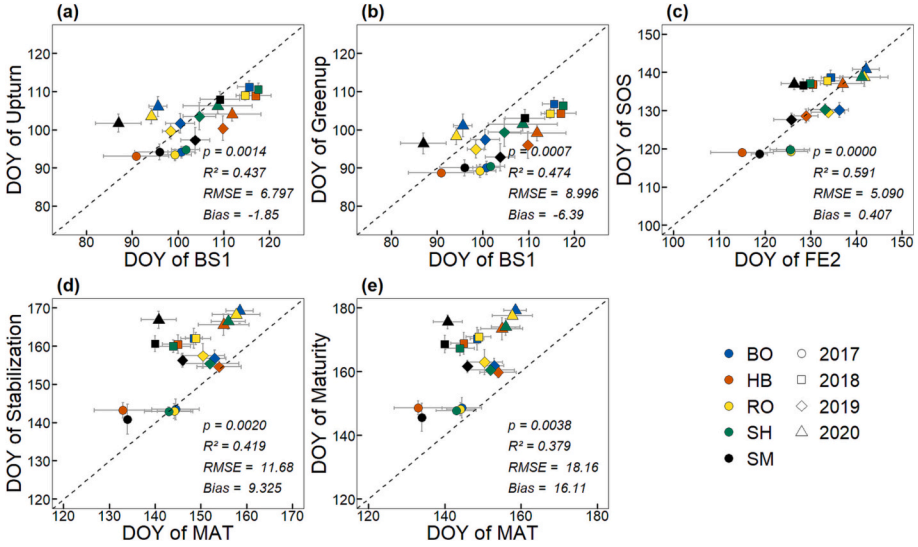

Fig. 15. The mean DOY of five curve feature-based satellite events (i.e., Gu-upturn, curvature-greenup, derivative-SOS, Gu-Stabilization, and curvature-maturity) approximated by the mean DOY of corresponding field events (i.e., budswell 1, budswell 1, leaf expansion 2, mature, and mature) per species and year using the calibrated PlanetScope data. Each satellite event is approximated by the field event with the lowest RMSE. Vertical and horizontal error bars represent one standard deviation of DOY of satellite events and field events, respectively. Species each have >5 large individuals, including BO – *Q. macrocarpa*, HB – *C. occidentalis*, RO – *Q. rubra*, SH – *C. laciniosa*, SM - *A. saccharum*.

estimates from the stabilization and maturity events may partly be due to the continued increase of leaf chlorophyll content after the visually observed maturity status of tree leaves (Keenan et al., 2014a, 2014b). Similar to threshold-based phenophase estimates, the curve feature-based phenophase estimates using the calibrated PlanetScope data yield consistently higher R^2 and mostly lower RMSE values than those estimates from the original PlanetScope data (Fig. S2).

Among all five satellite events, the derivative-based SOS can be more accurately used to estimate the corresponding field event (e.g., FE2), showing the stronger potential of satellite imagery in remotely detecting this leaf expansion event in spring. The derivative-based SOS can also be connected with the field events BB3 and FE1 with R^2 >0.8, indicating that variation in the mean phenological timing of leaf out and early leaf expansion can be captured even more by that of the derivative-based SOS, yet with larger RMSE and bias (Fig. S3). Similar to threshold-based analysis, the leaf out and expansion events can be characterized more accurately by the satellite event (i.e., derivative-based SOS) in comparison with the budswell event in the early season or the maturity event in the late spring. With a diversity of satellite events extracted from the four phenological metric extraction methods, all target field events throughout the spring tree leaf phenological development trajectory can be estimated, yet with varying degrees of accuracy.

4.6. Effect of tree-crown size on phenological event detection

For each tree crown of all 123 individuals, we calculate the difference in DOY between the field events and the corresponding satellite events (satellite-field event correspondence shown in Fig. 13 and Fig. 15). The difference is aggregated by species across years with mean and standard deviation calculated, which are further analyzed as a function of the species' mean tree-crown area (Fig. 16 and Fig. 17). For the species consisting mainly of small trees with crown sizes <90 m^2, the difference between the timing of field and corresponding satellite events varies widely, ranging from −20 to 20 days using the threshold-based method (Fig. 16). However, for the species consisting mainly of large trees (crown sizes >90 m^2), the difference between the timing of field and corresponding satellite events is closer to 0. With the increase of tree-crown size, the satellite events achieve better congruence with corresponding field events, leading to more consistent event-DOY difference with smaller fluctuations among species. The decreasing fluctuations between the satellite- and field event-difference indicate the potential of calibrated PlanetScope imagery in characterizing the crown-scale leaf phenological dynamics of large individuals. However, the detection of small tree-crown phenology is more uncertain, partly due to the potential mixed tree crowns within a PlanetScope pixel and

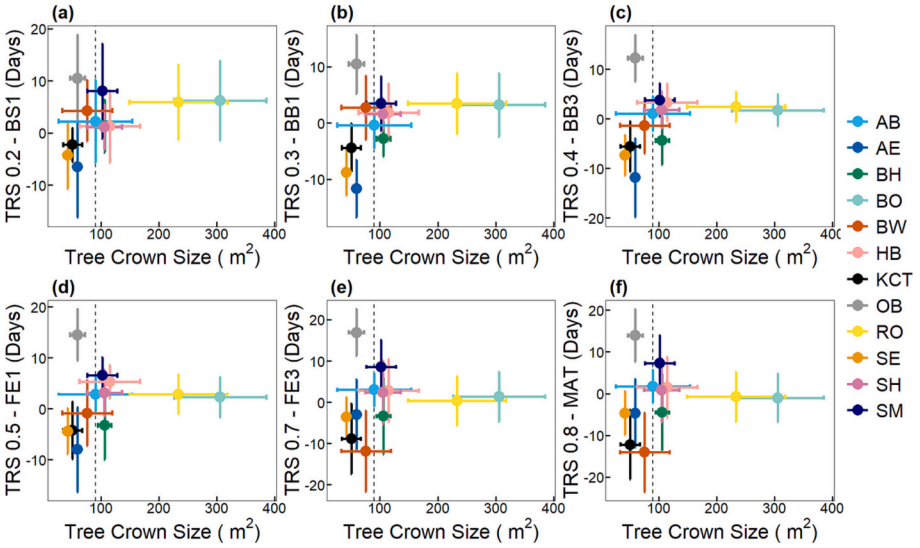

Fig. 16. The difference in days between the mean DOY of field and corresponding satellite events against the mean tree-crown area of each tree species in Trelease Woods. The error bar represents one standard deviation.

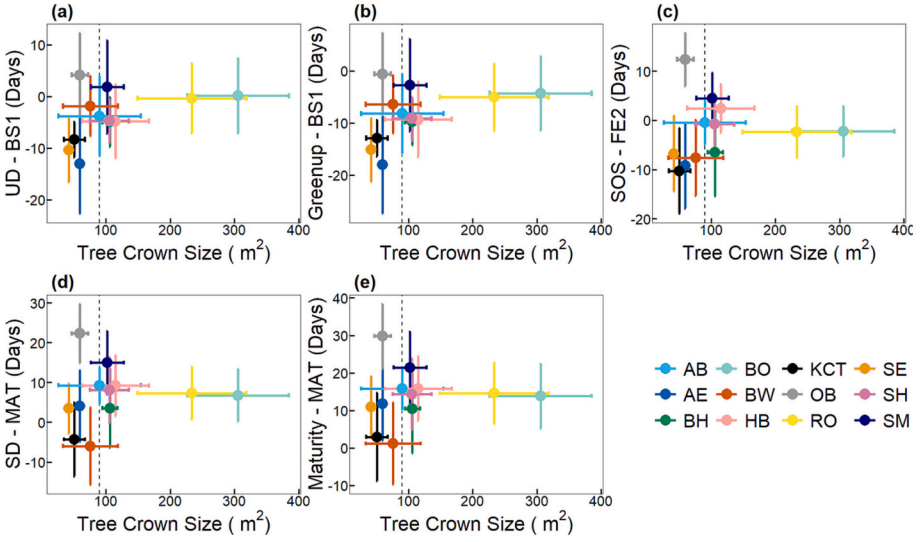

Fig. 17. The difference in days between the mean DOY of curve feature-based satellite events and corresponding field events against the mean tree-crown area of each tree species in Trelease Woods. The error bar represents one standard deviation.

increased requirement of radiometric sensitivity of satellite sensor to the spectral changes across tree crowns.

For the curve feature-based satellite events, similar patterns can be found in the date difference between each satellite and corresponding field events (Fig. 17). An increase in tree-crown size leads to more consistent date difference with smaller variation across species. Similar to Fig. 15, the Gu-based upturn and curvature-based greenup estimates tend to be earlier than the beginning of tree budswell for most species. The Gu-based stabilization and curvature-based maturity estimates generally are later than the field-observed tree maturity timing (Fig. 17). The PlanetScope-based tree leaf phenology detection accuracy varies across tree-crown sizes, with more consistent and stable performance for larger individuals.

4.7. Spatiotemporal variation of satellite events of the forest fragment

Three important field events (i.e., BB1, FE1, and MAT), representing early budburst (leaf out), early leaf expansion, and maturity of a tree crown, are selected for the subsequent analysis. These field events are most closely related to 30%, 50%, and 80% thresholds of the calibrated EVI2 time series, respectively. Thus, we map the spatial distribution of the satellite events of 30%, 50%, and 80% thresholds in our fragmented forest site using the calibrated PlanetScope data from 2017 to 2020 (Fig. 18). All three satellite events exhibit spatial and temporal variation across tree crowns in the study site, with relatively early event timing in 2017 and delayed timing in 2018. The northwest to the center of the study site has relatively earlier timing of all three satellite events in 2017 and 2019. This area consists mainly of *Q. macrocarpa*, *C. occidentalis*, *Q. rubra*, and *A. saccharum* that tend to go into the budburst, leaf expansion, and mature phases relatively earlier in these two years. In 2017, several large trees (e.g., *Q. macrocarpa* and *Q. rubra*) in the southwest of the study site enter the budburst and leaf expansion phases early, which corresponds to the early detection of satellite events of thresholds 30% and 50% in this area using the calibrated PlanetScope imagery, respectively. We further calculate the mean and standard deviation of three satellite events of the study site, as well as their

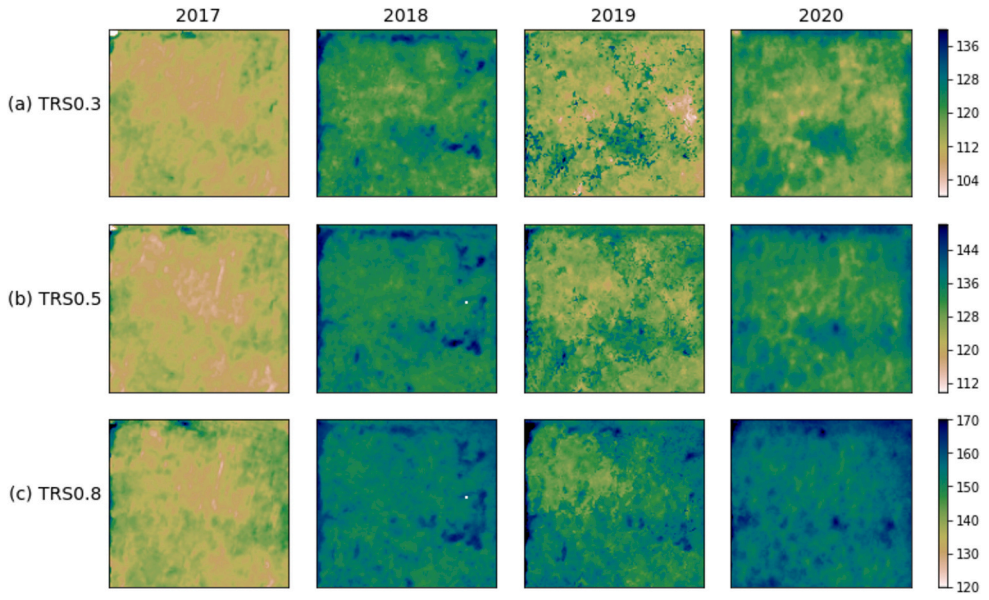

Fig. 18. Spatial variation maps of satellite events of 30%, 50% and 80% thresholds of our fragmented forest site from 2017 to 2020 using the calibrated PlanetScope imagery.

corresponding field events via sampled trees (Fig. 19). The comparable mean satellite-field event timing (the absolute difference of satellite and field event timing ranges from 0 to 7 days) demonstrates the strong potential of employing calibrated PlanetScope imagery in characterizing the crown-scale spring phenological trajectory of a fragmented forest. Among the four years, all satellite events have relatively earlier timing in 2017, in connection with the early start of field events BB1, FE1, and MAT in this year (Fig. 19). The satellite events of thresholds 30% and 50% are relatively delayed in 2018 and 2020, corresponding to the late start of field events BB1 and FE1 of those two years. The delayed satellite event of threshold 80% in 2020 corresponds to the late tree maturity event observed in the field.

5. Discussion

In this study, we propose a tree-crown scale remote sensing phenological monitoring framework to retrieve critical spring leaf phenological events of individual trees in a forest fragment in heterogeneous landscapes. This framework integrates the multi-scale MODIS and HLS imagery for calibrating PlanetScope imagery, incorporates intensive field phenological observations of individual trees and drone imagery-delineated crown boundaries, as well as bridges the satellite- and field-based phenological measures of individual trees for remotely characterizing a diverse set of spring phenological events (e.g., bud-swell, budburst, leaf expansion, and leaf maturity events) at the tree crown scale.

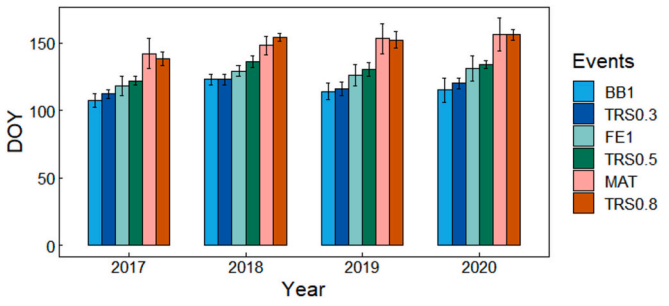

Fig. 19. Mean and standard deviation of three satellite events (i.e., thresholds 30%, 50% and 80%) of the study site, as well as their corresponding field events (i.e., BB1, FE1, and MAT) via sampled trees from 2017 to 2020.

The proposed phenological framework holds considerable significance in advancing tree leaf phenology detection of forest fragments using PlanetScope imagery. The limited area of fragmented forests requires the novel and rigorous design of the calibration procedure of PlanetScope imagery. Our framework integrates the hybrid deep learning-based fusion model with histogram matching, providing an innovative solution to the challenge of cross-sensor inconsistency in PlanetScope data. By integrating the SRCNN and LSTM, the hybrid deep learning-based fusion model is advantageous in predicting rapid phenological changes among the imagery, a long-standing challenge in spatiotemporal image fusion, particularly in heterogenous landscapes. During the early spring, the images documenting the rapid change of leaf greenness associated with the start of season are usually subject to cloud contamination in the study site. The rapid phenological changes due to the limited HLS images can be adequately accommodated in the hybrid deep learning-based fusion model. The high agreements between the MODIS-HLS fusion images and reference HLS images via accuracy metrics further demonstrate the good performance of the fusion model. With the fusion images of daily temporal resolution and 30-m spatial resolution as the reference, all the PlanetScope images are calibrated with histogram matching for the fragmented forest area to reduce the radiometric inconsistency. The further comparative analysis between the fusion and MODIS images as the calibration reference indicates the importance of taking into account the landscape fragmentation in histogram construction, when the study site occupies only a small area in a mixed landscape. The calibration of PlanetScope images using MODIS images as the reference may work for monitoring the phenology of large forests, as shown in previous studies (Wang et al., 2020; Wu et al., 2021). However, in the fragmented forest setting, the inadequate selection of reference images that contain a mixture of land covers negatively affects the calibration results. The use of fusion reference images in this study eliminates the influence of surrounding agriculture and ensures that the PlanetScope data are calibrated based on only the reflectance information of the same land cover type. The calibration technique devised for PlanetScope data in our framework can potentially be utilized for a wide range of fine-scale remote sensing applications beyond tree leaf phenology detection, particularly in heterogeneous landscapes.

Under the devised framework, we conduct intensive field phenological observations of 123 representative individual trees of 12 deciduous tree species in Trelease Woods throughout the spring season over

four years. For each individual tree, we record ten field phenological events of four phenological phases, ranging from budswell to leaf maturity phases, with a systematic and consistent in-situ phenological monitoring protocol. The field phenological observations also cover trees of varying crown sizes, with 42% being large individuals. We further collect a multitude of drone images spanning the growing season to delineate the tree crown boundary of each individual with the consideration of its GPS location, tree color tone, texture, spatial structure, morphology, as well as tree field measures and phenological observations. The integration of drone imagery-delineated tree crown boundaries and systematic in-situ phenological observations of individual trees is a key and indispensable step to building a comprehensive crown-scale ground phenological reference for validating satellite-derived tree phenological measures. The relevant field efforts are still rare in phenological studies, as most previous field efforts are limited by the number of trees sampled or the number of phenological events observed with a consistent protocol (Berra and Gaulton, 2021; Fisher et al., 2006; Kowalski et al., 2020).

The framework successfully leverages the reflectance information in MODIS, HLS and PlanetScope data, and generates high quality 3-m EVI2 time series for leaf phenology detection. Importantly, all the key field events (i.e., BS1, BB1, BB3, FE1, FE3, and MAT) throughout the spring season are successfully approximated by corresponding satellite events, especially for large individuals. This comprehensive phenological characterization notably expands the limited spring field event detected by remote sensing in previous studies, which mostly focus on the field event of budburst (leaf out) at the landscape level (Berra and Gaulton, 2021; Kang et al., 2003; Khare et al., 2019). Among the phenological metric extraction methods, the threshold-based method demonstrates enhanced capability to identify subtle leaf phenological changes in spring, with BS1, BB1, BB3, FE1, FE3 and MAT field events bridged to the 20%, 30%, 40%, 50%, 70% and 80% thresholds of EVI2 time series, respectively. As for the curve feature-based satellite events, the Gu-based upturn and curvature-based greenup events approximate the field event BS1. The derivative-based SOS event corresponds with the field event FE2. The Gu-based stabilization and curvature-based maturity events are connected to the field event MAT. The field phenological events of full leaf out and early leaf expansion (i.e., BB3 and FE1) can be bridged to corresponding satellite events (i.e., 40% and 50% thresholds) with high accuracy. In the early spring, the weak signal of budswell is harder to be captured by the satellite imagery, and the detection of early field events (e.g., BS1) is more subject to the influence of understory phenology, soil background, and snow contamination. For example, the mean emergence timing of understory herbs in the study site from 2017 to 2020 is about DOY 98 (standard deviation of 5.5 days), which is around the budswell phase for tree crowns (Augspurger and Zaya, 2020). At the end of spring, the subtle phenological change from leaf expansion to maturity makes the remote detection of corresponding field events (i.e., FE3 and MAT) more difficult. With the comprehensive analysis of both field and satellite events, the framework corroborates not only the conventional limited, satellite-field event bridging relationship at the landscape level of previous studies (i.e., forest leaf out onset timing approximated by 20–30% threshold of vegetation index time series), but also successfully broadens the scope of phenological detection from limited field events to a range of critical ones throughout the tree spring phenological development trajectory (Bórnez et al., 2020; Klosterman et al., 2018; Kowalski et al., 2020; Xie and Wilson, 2020).

The framework enables the monitoring of the staggering phenological development among individual trees within a forest fragment. Among the trees of various crown sizes, the tree-crown scale leaf phenology can be detected more accurately for large individuals using the PlanetScope imagery. With those large individuals mostly from dominant species, leaf phenology monitoring throughout the spring season can further improve our understanding of how those species, as well as the associated fragmented forest, respond to climate and environmental changes. Large trees and dominant species are vital to an ecosystem, as large trees make up most of the above-ground biomass and provide important habitats for animals, while dominant tree species influence the diversity of herbivores and forest productivity (Kim and Choi, 2021; Lutz et al., 2018). The phenological monitoring of those trees and species helps to identify the ones sensitive to environmental disturbances in a fragmented environment, as well as adapt the forest management to climate change. Furthermore, the thorough detection of a range of field phenological events enables the quantification of tree spring phenological development rate and phase duration, as well as helps to assess the influence of environmental changes on different phenological phases (e.g., budswell, budburst, leaf expansion, and leaf maturity phases), which usually have distinct ecological and biological implications. The different spatiotemporal phenological variation patterns of different satellite events in the study site (Fig. 18) also indicate the importance and benefit of the phase-specific assessment.

Despite the valuable insights provided by our study in monitoring tree leaf phenology of forest fragments, it also has limitations. One limitation is associated with the use of PlanetScope imagery in detecting small tree crown phenology, which may potentially bring uncertainties due to the mixed tree crowns within a PlanetScope pixel and increased requirement of radiometric sensitivity of satellite sensor to the spectral changes across tree crowns. As a consequence, the spring leaf phenology of large trees can be more accurately detected than that of small tree crowns. The further integration of time series of drone imagery with the calibrated PlanetScope imagery may help improve the accuracy of leaf phenological change detection of small trees. Another limitation lies in the scale of in-situ phenological data. While our systematic tree field phenological observations are key to bridging a diversity of satellite-field phenological events, the in-situ tree phenological observations at our study site (i.e., Trelease Woods) may not well capture the diversity of phenological responses across different habitat types and microclimates. The in-situ and remotely sensed phenology also differs in observation angles, with the in-situ phenology observed at the ground level by looking upward into the canopy and the remotely sensed phenology detected from satellite views above the canopy. In the future, it would be valuable to explore the incorporation of phenological camera networks (e.g., North American PhenoCam Network) distributed across a wide range of habitats with more comparable phenological views, despite the caveats concerning the limited trees recorded under the camera field of view (Richardson et al., 2018a; Seyednasrollah et al., 2019). Citizen science initiatives (e.g., US National Phenology Network) and crowdsourcing platforms could also be utilized to expand the spatial coverage of in-situ phenological data with consistent observing protocols (Peng et al., 2017a, 2017b). With the expanded in-situ data, the framework can be tested further in forest fragments of various species composition across habitats for evaluating the satellite-field event bridging relationship at the tree-crown scale. To expand the scope of this study to larger areas, manual delineation of crown boundaries may be time-consuming and subject to the influence of observer delineation experience and skills. Automatic image segmentation may be employed to help reduce the amount of time required to delineate boundaries as well as enhance consistency and repeatability of crown delineation. Given the importance of tree crown boundaries in subsequent phenology monitoring, the performance of automatic segmentation methods needs to be evaluated, particularly in complex forests where tree crowns are overlapping or irregular, or trees vary significantly in size, shape, and species.

In general, the tree-crown scale phenological monitoring framework proposed in this study enables the monitoring of a multitude of spring leaf phenological events of individual trees in a forest fragment. In the future, the framework can be tested further in forest fragments with a lower density of herbs and/or saplings to explore the effects of understory on detecting the field events in the early spring. As the phenological change from leaf expansion to maturity is more subtle at the end of spring, the characterization of these field events in the future might

benefit from the further integration of other vegetation indices, such as wide dynamic range vegetation index (WDRVI) and MERIS terrestrial chlorophyll index (MTCI) (Dash and Curran, 2007; Gitelson, 2004). These indices are sensitive to the change of chlorophyll content, particularly in high chlorophyll values. The monitoring of all the key spring phenological events at the tree-crown scale is critical for enhancing our understanding of tree species phenological responses to environmental disturbance and climate change, aiding in more effective forest management and conservation.

6. Conclusions

Forest fragmentation has been continually exacerbated by the expansion of urban and agricultural fields in recent years. Forest fragments, despite limited sizes, have important ecosystem functions and are more sensitive to environmental disturbances than intact forests. Tree leaf phenology is an important indicator to monitor the influence of climate or environmental changes on forest fragments. In this study, we propose a tree-crown scale remote sensing phenological monitoring framework to detect a diversity of spring phenological events of individual trees of a forest fragment in heterogenous landscapes. This framework consists of four components: high spatiotemporal resolution fusion imagery generation with multi-scale satellite time series, PlanetScope imagery calibration with the fusion data, tree-crown scale phenology trajectory modeling, and tree-crown scale phenological event characterization and assessment. The results demonstrate that calibrating PlanetScope imagery with high-quality MODIS-HLS fusion data can reduce effectively the cross-sensor radiometric inconsistency as well as the fluctuations in EVI2 time series, thus improving the accuracy of spring phenological event detection of individual trees. The further comparative analysis between the fusion and MODIS images as the calibration reference infers the importance of taking into account the landscape fragmentation in PlanetScope imagery calibration, particularly for fragmented forests in heterogeneous landscapes. The framework successfully characterizes all the key spring phenological events (e.g., budswell, budburst, leaf expansion, and leaf maturity events) of individual trees of our study site, with leaf out and early leaf expansion events retrieved with high accuracy, particularly for large tree crowns. The developed framework not only broadens the horizon of leaf phenological monitoring from the landscape to tree-crown scales, but also expands the scope of phenological detection from limited field events to a range of critical ones throughout the tree spring phenological development trajectory. The monitoring of all the key spring phenological events of individual trees will shed light on tree species phenological responses to environmental and climate change, further facilitating the identification of species vulnerable to environmental disturbances and assessment of potential shifts in species distributions under climate change.

CRediT authorship contribution statement

Yilun Zhao: Conceptualization, Data curation, Formal analysis, Investigation, Methodology, Software, Validation, Visualization, Writing – original draft. **Chunyuan Diao:** Conceptualization, Funding acquisition, Investigation, Methodology, Project administration, Resources, Supervision, Writing – review & editing. **Carol K. Augspurger:** Conceptualization, Data curation, Investigation, Methodology, Writing – review & editing. **Zijun Yang:** Formal analysis, Investigation, Methodology, Writing – review & editing.

Declaration of Competing Interest

The authors declare that they have no known competing financial interests or personal relationships that could have appeared to influence the work reported in this paper.

Data availability

Data will be made available on request.

Acknowledgements

This work is supported by the National Science Foundation under Grant 1951657 and the National Aeronautics and Space Administration under Grant 80NSSC22K1548. We also thank the University of Illinois at Urbana-Champaign and National Center for Supercomputing Applications for providing the Blue Waters computational resources to generate the fusion data. We would also like to thank two reviewers for their valuable comments and suggestions.

Appendix A. Supplementary data

Supplementary data to this article can be found online at https://doi.org/10.1016/j.rse.2023.113790.

References

Aguilar-Melo, A.R., Andresen, E., Cristóbal-Azkarate, J., Arroyo-Rodríguez, V., Chavira, R., Schondube, J., Serio-Silva, J.C., Cuarón, A.D., 2013. Behavioral and physiological responses to subgroup size and number of people in howler monkeys inhabiting a forest fragment used for nature-based tourism. Am. J. Primatol. 75, 1108–1116. https://doi.org/10.1002/AJP.22172.

Ahrends, H.E., Etzold, S., Kutsch, W.L., Stoeckli, R., Bruegger, R., Jeanneret, F., Wanner, H., Buchmann, N., Eugster, W., 2009. Tree phenology and carbon dioxide fluxes: use of digital photography for process-based interpretation at the ecosystem scale. Clim. Res. 39, 261–274. https://doi.org/10.3354/cr00811.

Amaya-Espinel, J.D., Hostetler, M.E., 2019. The value of small forest fragments and urban tree canopy for neotropical migrant birds during winter and migration seasons in latin american countries: a systematic review. Landsc. Urban Plan. 190, 103592 https://doi.org/10.1016/J.LANDURBPLAN.2019.103592.

Augspurger, C.K., Zaya, D.N., 2020. Concordance of long-term shifts with climate warming varies among phenological events and herbaceous species. Ecol. Monogr. 90, e01421.

Augspurger, C.K., Zaya, D.N., 2022. Woody phenology and weather data related to Trelease Woods, Urbana, IL, USA 1993-2022. https://doi.org/10.5061/dryad.3j9kd51p1.

Beck, Pieter S.A., Atzberger, C., Høgda, K.A., Johansen, B., Skidmore, A.K., 2006. Improved monitoring of vegetation dynamics at very high latitudes: a new method using MODIS NDVI. Remote Sens. Environ. 100, 321–334. https://doi.org/10.1016/j.rse.2005.10.021.

Berra, E.F., Gaulton, R., 2021. Remote sensing of temperate and boreal forest phenology: A review of progress, challenges and opportunities in the intercomparison of in-situ and satellite phenological.

Bolton, D.K., Gray, J.M., Melaas, E.K., Moon, M., Eklundh, L., Friedl, M.A., 2020. Continental-scale land surface phenology from harmonized landsat 8 and Sentinel-2 imagery. Remote Sens. Environ. 240, 111685.

Bórnez, K., Descals, A., Verger, A., Peñuelas, J., 2020. Land surface phenology from VEGETATION and PROBA-V data. Assessment over deciduous forests. Int. J. Appl. Earth Obs. Geoinf. 84 https://doi.org/10.1016/J.JAG.2019.101974.

Bryan-Brown, D.N., Connolly, R.M., Richards, D.R., Adame, F., Friess, D.A., Brown, C.J., 2020. Global trends in mangrove forest fragmentation. Sci. Rep. 10 https://doi.org/10.1038/s41598-020-63880-1.

Cao, R., Chen, J., Shen, M., Tang, Y., 2015. An improved logistic method for detectingspring vegetation phenology in grasslands from MODIS EVI time-series data. Agric.For. Meteorol. 200, 9–20.

Chaithra, C.C., Taranath, N.L., Darshan, L.M., Subbaraya, C.K., 2018. A survey on image fusion techniques and performance metrics. In: 2018 Second International Conference on Electronics, Communication and Aerospace Technology (ICECA). IEEE, pp. 995–999.

Chang, M., 2006. Forest hydrology: an introduction to water and forests. CRC Press.

Chen, J., Jönsson, P., Tamura, M., Gu, Z., Matsushita, B., Eklundh, L., 2004. A simple method for reconstructing a high-quality NDVI time-series data set based on the Savitzky–Golay filter. Remote Sens. Environ. 91 (3–4), 332–344.

Chen, Z., Wang, L., Dai, Y., Wan, X., Liu, S., 2017. Phenology-dependent variation in the non-structural carbohydrates of broadleaf evergreen species plays an important role in determining tolerance to defoliation (or herbivory) OPEN. Sci. Rep. 7 https://doi.org/10.1038/s41598-017-09757-2.

Claverie, M., Ju, J., Masek, J.G., Dungan, J.L., Vermote, E.F., Roger, J.-C., Skakun, S.V., Justice, C., 2018. The Harmonized Landsat and Sentinel-2 surface reflectance data set. Remote Sens. Environ. 219, 145–161.

Curtis, P.G., Slay, C.M., Harris, N.L., Tyukavina, A., Hansen, M.C., 2018. Classifying drivers of global forest loss. Science 1979 (361), 1108–1111. https://doi.org/10.1126/SCIENCE.AAU3445/SUPPL_FILE/AAU3445_CURTIS_SM.PDF.

Dai, J., Wang, H., Ge, Q., 2014. The spatial pattern of leaf phenology and its response to climate change in China. International journal of biometeorology 58, 521–528.

Dash, J., Curran, P.J., 2007. Evaluation of the MERIS terrestrial chlorophyll index (MTCI). Adv. Space Res. 39, 100–104. https://doi.org/10.1016/J.ASR.2006.02.034.
Diao, C., 2020. Remote sensing phenological monitoring framework to characterize corn and soybean physiological growing stages. Remote Sens. Environ. 248, 111960.
Diao, C., 2019. Complex network-based time series remote sensing model in monitoring the fall foliage transition date for peak coloration. Remote Sens. Environ. 229, 179–192.
Diao, C., Li, G., 2022. Near-surface and high-resolution satellite time series for detecting crop phenology. Remote Sens. 14, 1957.
Donnelly, A., Yu, R., Caffarra, A., Hanes, J., Liang, L., Desai, A.R., Liu, L., Schwartz, M.D., 2017. Interspecific and interannual variation in the duration of spring phenophases in a northern mixed forest. Agric. For. Meteorol. 243, 55–67. https://doi.org/10.1016/j.agrformet.2017.05.007.
dos Santos, A.R., Araújo, E.F., Barros, Q.S., Fernandes, M.M., de Moura Fernandes, M.R., Moreira, T.R., de Souza, K.B., da Silva, E.F., Silva, J.P.M., Santos, J.S., Billo, D., Silva, R.F., Nascimento, G.S.P., da Silva Gandine, S.M., Pinheiro, A.A., Ribeiro, W.R., Gonçalves, M.S., da Silva, S.F., Senhorelo, A.P., Heitor, F.D., Berude, L.C., de AlmeidaTelles, L.A., 2020. Fuzzy concept applied in determining potential forest fragments for deployment of a network of ecological corridors in the brazilian Atlantic Forest. Ecol. Indic. 115, 106423 https://doi.org/10.1016/J.ECOLIND.2020.106423.
Dronova, I., Taddeo, S., 2022. Remote sensing of phenology: towards the comprehensive indicators of plant community dynamics from species to regional scales. J. Ecol. 110, 1460–1484.
Elmore, A.J., Guinn, S.M., Minsley, B.J., Richardson, A.D., 2012. Landscape controls on the timing of spring, autumn, and growing season length in mid-Atlantic forests. Global Change Biol 18, 656–674.
Evans, E.W., Carlile, N.R., Innes, M.B., Pitigala, N., 2012. Warm springs reduce parasitism of the cereal leaf beetle through phenological mismatch. J. Appl. Entomol. 137, 383–391. https://doi.org/10.1111/jen.12028.
Fawcett, D., Bennie, J., Anderson, K., 2021. Monitoring spring phenology of individual tree crowns using drone-acquired NDVI data. Remote Sens. Ecol. Conserv. 7, 227–244.
Fernando, L., Magnago, S., Ferreira Rocha, M., Meyer, L., Martins, V., Augusto, J., Meira-Neto, A., 2015. Microclimatic conditions at forest edges have significant impacts on vegetation structure in large Atlantic forest fragments. Biodivers. Conserv. 24, 2305–2318. https://doi.org/10.1007/s10531-015-0961-1.
Filippa, G., Cremonese, E., Migliavacca, M., Galvagno, M., Forkel, M., Wingate, L., Tomelleri, E., Morra di Cella, U., Richardson, A.D., 2016. Phenopix: a R package for image-based vegetation phenology. Agric. For. Meteorol. 220, 141–150. https://doi.org/10.1016/j.agrformet.2016.01.006.
Fisher, J.I., Mustard, J.F., Vadeboncoeur, M.A., 2006. Green leaf phenology at landsat resolution: scaling from the field to the satellite. Remote Sens. Environ. 100, 265–279. https://doi.org/10.1016/j.rse.2005.10.022.
Flynn, D.F.B., Wolkovich, E.M., 2018. Temperature and photoperiod drive spring phenology across all species in a temperate forest community. New Phytol. 219, 1353–1362. https://doi.org/10.1111/nph.15232.
Frazier, A.E., Hemingway, B.L., 2021. A technical review of planet smallsat data: practical considerations for processing and using planetscope imagery. Remote Sens. 13 https://doi.org/10.3390/rs13193930.
Fridley, J.D., 2012. Extended leaf phenology and the autumn niche in deciduous forest invasions. Nature 485, 359–362. https://doi.org/10.1038/nature11056.
Galvão, L.S., dos Santos, J.R., Roberts, D.A., Breunig, F.M., Toomey, M., de Moura, Y.M., 2011. On intra-annual EVI variability in the dry season of tropical forest: a case study with MODIS and hyperspectral data. Remote Sens. Environ. 115, 2350–2359. https://doi.org/10.1016/J.RSE.2011.04.035.
Gao, F., Anderson, M.C., Zhang, X., Yang, Z., Alfieri, J.G., Kustas, W.P., Mueller, R., Johnson, D.M., Prueger, J.H., 2017. Toward mapping crop progress at field scales through fusion of landsat and MODIS imagery. Remote Sens. Environ. 188, 9–25.
Gibson, L., Lynam, A.J., Bradshaw, C.J.A., He, F., Bickford, D.P., Woodruff, D.S., Bumrungsri, S., Laurance, W.F., 2013. Near-complete extinction of native small mammal fauna 25 years after forest fragmentation. Science 1979 (341), 1508–1510. https://doi.org/10.1126/SCIENCE.1240495/SUPPL_FILE/GIBSON.SM.PDF.
Gitelson, A.A., 2004. Wide dynamic range vegetation index for remote quantification of biophysical characteristics of vegetation. J. Plant Physiol. 161, 165–173. https://doi.org/10.1078/0176-1617-01176.
Gu, L., Post, W.M., Baldocchi, D.D., Black, T.A., Suyker, A.E., Verma, S.B., Vesala, T., Wofsy, S.C., 2009. Characterizing the seasonal dynamics of plant community photosynthesis across a range of vegetation types. In: Phenology of Ecosystem Processes: Applications in Global Change Research, pp. 35–58.
Hofmeister, J., Hošek, J., Brabec, M., Střalková, R., Mýlová, P., Bouda, M., Pettit, J.L., Rydval, M., Svoboda, M., 2019. Microclimate edge effect in small fragments of temperate forests in the context of climate change. For. Ecol. Manag. 448, 48–56. https://doi.org/10.1016/J.FORECO.2019.05.069.
Houborg, R., McCabe, M.F., 2018. A cubesat enabled spatio-temporal enhancement method (CESTEM) utilizing planet, landsat and MODIS data. Remote Sens. Environ. 209, 211–226. https://doi.org/10.1016/j.rse.2018.02.067.
Huete, A., Didan, K., Miura, T., Rodriguez, E.P., Gao, X., Ferreira, L.G., 2002. Overview of the radiometric and biophysical performance of the MODIS vegetation indices. Remote Sens. Environ. 83, 195–213.
Jiang, Z., Huete, A.R., Didan, K., Miura, T., 2008. Development of a two-band enhanced vegetation index without a blue band. Remote Sens. Environ. 112 (10), 3833–3845. https://doi.org/10.1016/j.rse.2008.06.006.
Jönsson, P., Eklundh, L., 2004. TIMESAT—a program for analyzing time-series of satellite sensor data. Comput. Geosci. 30, 833–845.
Kang, S., Running, S.W., Lim, J.-H., Zhao, M., Park, C.-R., Loehman, R., 2003. A regional phenology model for detecting onset of greenness in temperate mixed forests, Korea: an application of MODIS leaf area index. Remote Sens. Environ. 86, 232–242.
Keenan, T.F., Darby, B., Felts, E., Sonnentag, O., Friedl, M.A., Hufkens, K., O'Keefe, J., Klosterman, S., Munger, J.W., Toomey, M., Richardson, A.D., 2014. Tracking forest phenology and seasonal physiology using digital repeat photography: a critical assessment. Ecol. Appl. 24, 1478–1489. https://doi.org/10.1890/13-0652.1.
Keenan, Trevor F., Gray, J., Friedl, M.A., Toomey, M., Bohrer, G., Hollinger, D.Y., Munger, J.W., O'Keefe, J., Schmid, H.P., Wing, I.S., Yang, B., Richardson, A.D., 2014. Net carbon uptake has increased through warming-induced changes in temperate forest phenology. Nat. Clim. Chang 4. https://doi.org/10.1038/NCLIMATE2253.
Khare, S., Drolet, G., Sylvain, J.-D., Paré, M.C., Rossi, S., 2019. Assessment of spatio-temporal patterns of black spruce bud phenology across Quebec based on MODIS-NDVI time series and field observations. Remote Sens. 11 https://doi.org/10.3390/rs11232745.
Kim, N.-H., Choi, S.-W., 2021. Role of dominant tree species on diversity of herbivorous insect community in temperate forests. J. Asia Pac. Entomol. 24, 1226–8615. https://doi.org/10.1016/j.aspen.2021.01.010.
Klosterman, S., Melaas, E., Wang, J., Martinez, A., Frederick, S., O'Keefe, J., Orwig, D.A., Wang, Z., Sun, Q., Schaaf, C., Friedl, M., Richardson, A.D., 2018. Fine-scale perspectives on landscape phenology from unmanned aerial vehicle (UAV) photography. Agric. For. Meteorol. 248, 397–407. https://doi.org/10.1016/j.agrformet.2017.10.015.
Klosterman, S.T., Hufkens, K., Gray, J.M., Melaas, E., Sonnentag, O., Lavine, I., Mitchell, L., Norman, R., Friedl, M.A., Richardson, A.D., 2014. Evaluating remote sensing of deciduous forest phenology at multiple spatial scales using PhenoCam imagery. Biogeosciences 11, 4305–4320. https://doi.org/10.5194/bg-11-4305-2014.
Kowalski, K., Senf, C., Hostert, P., Pflugmacher, D., 2020. Characterizing spring phenology of temperate broadleaf forests using landsat and Sentinel-2 time series. Int. J. Appl. Earth Obs. Geoinf. 92 https://doi.org/10.1016/J.JAG.2020.102172.
Liu, Z.-G., Li, K., Cai, Y.-L., Fang, Y., 2011. Correlations between leafing phenology and traits: Woody species of evergreen broad-leaved forests in subtropical China. Pol. J. Ecol. 59, 463–473.
Lutz, J.A., Furniss, T.J., Johnson, D.J., Davies, S.J., Allen, D., Alonso, A., Anderson-Teixeira, K.J., Andrade, A., Baltzer, J., Becker, L., Blomdahl, E.M., Bourg, N.A., Bunyavejchewin, S., Burslem, R.P., Alina Cansler, C., Cao, K., Cao, M., Chang, L.-W., Chao, K.-J., Chao, W.-C., Chiang, J.-M., Chu, C., Chuyong, G.B., Clay, K., Condit, R., Cordell, S., Dattaraja, H.S., Duque, A., Ewango, N., Fischer, G.A., Fletcher, C., Freund, J.A., Giardina, C., Germain, S.J., Gilbert, G.S., Hao, Z., Hart, T., Hau, H., He, F., Hector, A., Howe, R.W., Hsieh, C.-F., Hu, Y.-H., Hubbell, S.P., Inman-Narahari, F.M., Itoh, A., Janík, D., Rahman Kassim, A., Kenfack, D., Korte, L., Larson, A.J., Li, Y., Lin, Y., Liu, S., Lum, S., Ma, K., Makana, J.-R., Malhi, Y., McMahon, S.M., McShea, W.J., Memiaghe, H.R., Mi, X., Morecroft, M., Musili, P.M., Myers, J.A., Novotny, V., de Oliveira, A., Ong, P., Orwig, D.A., Ostertag, R., Parker, G.G., Patankar, R., Phillips, R.P., Reynolds, G., Sack, L., Song, G.-Z.M., Su, S.-H., Sukumar, R., Sun, I.-F., Suresh, H.S., Swanson, M.E., Tan, S., Thomas, D.W., Thompson, J., Uriarte, M., Valencia, R., Vicentini, A., Wang, X., Weiblen, G.D., Wolf, A., Wu, S.-H., Xu, H., Yamakura, T., Yap, S., Zimmerman, J.K., 2018. Global importance of large-diameter trees, 7. https://doi.org/10.1111/geb.12747.
Matongera, T.N., Mutanga, O., Sibanda, M., Odindi, J., 2021. Estimating and monitoring land surface phenology in rangelands: a review of progress and challenges. Remote Sens. 13, 2060.
Meier, I.C., Leuschner, C., 2008. Leaf size and leaf area index in Fagus sylvatica forests: competing effects of precipitation, temperature, and nitrogen availability. Ecosystems 11, 655–669. https://doi.org/10.1007/s10021-008-9135-2.
Morin, X., Roy, J., Sonié, L., Chuine, I., 2010. Changes in leaf phenology of three European oak species in response to experimental climate change. New Phytologist 186 (4), 900–910.
Morton, D.C., Nagol, J., Carabajal, C.C., Rosette, J., Palace, M., Cook, B.D., Vermote, E.F., Harding, D.J., North, P.R.J., 2014. Amazon forests maintain consistent canopy structure and greenness during the dry season. Nature 506, 221–224. https://doi.org/10.1038/nature13006.
Öztürk, M., Bolat, I., Ergün, A., 2015. Influence of air–soil temperature on leaf expansion and LAI of Carpinus betulus trees in a temperate urban forest patch. Agric. For. Meteorol. 200, 185–191. https://doi.org/10.1016/J.AGRFORMET.2014.09.014.
Panchen, Z.A., Primack, R.B., Nordt, B., Ellwood, E.R., Stevens, A.-D., Renner, S.S., Willis, C.G., Fahey, R., Whittemore, A., Du, Y., Davis, C.C., Primack, R., 2014. Leaf out times of temperate woody plants are related to phylogeny, deciduousness, growth habit and wood anatomy. New Phytol. 203, 1208–1219. https://doi.org/10.1111/nph.12892.
Peng, D., Wu, C., Li, C., Zhang, X., Liu, Z., Ye, H., Luo, S., Liu, X., Hu, Y., Fang, B., 2017a. Spring green-up phenology products derived from MODIS NDVI and EVI: intercomparison, interpretation and validation using National Phenology Network and AmeriFlux observations. Ecol. Indic. 77, 323–336. https://doi.org/10.1016/j.ecolind.2017.02.024.
Peng, D., Zhang, X., Wu, C., Huang, W., Gonsamo, A., Huete, A.R., Didan, K., Tan, B., Liu, X., Zhang, B., 2017b. Intercomparison and evaluation of spring phenology products using National Phenology Network and AmeriFlux observations in the contiguous United States. Agric. For. Meteorol. 242, 33–46. https://doi.org/10.1016/j.agrformet.2017.04.009.
Planet Imagery Product Specifications. Planet Labs, 2020. Inc, San Francisco, CA, USA.
Reed, B.C., Schwartz, M.D., Xiao, X., 2009. Remote sensing phenology. In: Noormets, A. (Ed.), Phenology of Ecosystem Processes: Applications in Global Change Research.

Springer, New York, New York, NY, pp. 231–246. https://doi.org/10.1007/978-1-4419-0026-5_10.
Richardson, A.D., Hufkens, K., Milliman, T., Aubrecht, D.M., Chen, M., Gray, J.M., Johnston, M.R., Keenan, T.F., Klosterman, S.T., Kosmala, M., Melaas, E.K., Friedl, M. A., Frolking, S., 2018a. Tracking vegetation phenology across diverse north american biomes using PhenoCam imagery. Sci. Data 5, 180028. https://doi.org/10.1038/sdata.2018.28.
Richardson, A.D., Hufkens, K., Milliman, T., Aubrecht, D.M., Furze, M.E., Seyednasrollah, B., Krassovski, M.B., Latimer, J.M., Robert Nettles, W., Heiderman, R.R., Warren, J.M., Hanson, P.J., 2018. Ecosystem warming extends vegetation activity but heightens vulnerability to cold temperatures. https://doi.org/10.1038/s41586-018-0399-1.
Saleska, S.R., Wu, J., Guan, K., Araujo, A.C., Huete, A., Nobre, A.D., Restrepo-Coupe, N., 2016. Dry-season greening of Amazon forests. Nature 531, E4–E5. https://doi.org/10.1038/nature16457.
Seyednasrollah, B., Young, A.M., Hufkens, K., Milliman, T., Friedl, M.A., Frolking, S., Richardson, A.D., 2019. Tracking vegetation phenology across diverse biomes using version 2.0 of the PhenoCam dataset. Sci. Data 6, 222. https://doi.org/10.1038/s41597-019-0229-9.
Smith, L.M., 2013. Extended leaf phenology in deciduous forest invaders: mechanisms of impact on native communities. J. Veg. Sci. 24, 979–987. https://doi.org/10.1111/JVS.12087.
Song, Z., Song, X., Pan, Y., Dai, K., Shou, J., Chen, Q., Huang, J., Tang, X., Huang, Z., Du, Y., 2020. Effects of winter chilling and photoperiod on leaf-out and flowering in a subtropical evergreen broadleaved forest in China. For. Ecol. Manag. 458, 117766 https://doi.org/10.1016/J.FORECO.2019.117766.
Sun, S., Jin, D., Li, R., 2006. Leaf emergence in relation to leaf traits in temperate woody species in east-chinese Quercus fabri forests. Acta Oecol. 30, 212–222. https://doi.org/10.1016/j.actao.2006.04.001.
Tan, B., Morisette, J.T., Wolfe, R.E., Gao, F., Ederer, G.A., Nightingale, J., Pedelty, J.A., 2010. An enhanced TIMESAT algorithm for estimating vegetation phenology metrics from MODIS data. IEEE J. Sel. Top. Appl. Earth Obs. Remote Sens. 4, 361–371.
Taubert, F., Fischer, R., Groeneveld, J., Lehmann, S., Müller, M.S., Rödig, E., Wiegand, T., Huth, A., 2018. Global patterns of tropical forest fragmentation. Nature 554 (7693), 519–522. https://doi.org/10.1038/nature25508.
Tyrväinen, L., Pauleit, S., Seeland, K., de Vries, S., 2005. Benefits and uses of urban forests and trees. In: Urban Forests and Trees. Springer, pp. 81–114.
van Vliet, J., 2019. Direct and indirect loss of natural area from urban expansion. Nat. Sustain. 2 (8), 755–763. https://doi.org/10.1038/s41893-019-0340-0.
van Wees, D., van der Werf, G.R., Randerson, J.T., Andela, N., Chen, Y., Morton, D.C., 2021. The role of fire in global forest loss dynamics. Glob. Chang. Biol. 27, 2377. https://doi.org/10.1111/GCB.15591.
Vrieling, A., Meroni, M., Darvishzadeh, R., Skidmore, A.K., Wang, T., Zurita-Milla, R., Oosterbeek, K., O'Connor, B., Paganini, M., 2018. Vegetation phenology from Sentinel-2 and field cameras for a dutch barrier island. Remote Sens. Environ. 215, 517–529.
Vrieling, A., Skidmore, A.K., Wang, T., Meroni, M., Ens, B.J., Oosterbeek, K., O'Connor, B., Darvishzadeh, R., Heurich, M., Shepherd, A., 2017. Spatially detailed retrievals of spring phenology from single-season high-resolution image time series. Int. J. Appl. Earth Obs. Geoinf. 59, 19–30.
Wang, J., Yang, D., Detto, M., Nelson, B.W., Chen, M., Guan, K., Wu, S., Yan, Z., Wu, J., 2020. Multi-scale integration of satellite remote sensing improves characterization of dry-season green-up in an Amazon tropical evergreen forest. Remote Sens. Environ. 246 https://doi.org/10.1016/j.rse.2020.111865.
White, M.A., Thornton, P.E., Running, S.W., 1997. A continental phenology model for monitoring vegetation responses to interannual climatic variability. Glob. Biogeochem. Cycles 11, 217–234.
Willis, C.G., Ruhfel, B.R., Primack, R.B., Miller-Rushing, A.J., Losos, J.B., 2010. Favorable climate change response explains non-native species' success in Thoreau's woods. PLoS One 5, 8878. https://doi.org/10.1371/journal.pone.0008878.
Wolkovich, E.M., Davies, T.J., Schaefer, H., Cleland, E.E., Cook, B.I., Travers, S.E., Willis, C.G., Davis, C.C., 2013. Temperature-dependent shifts in phenology contribute to the success of exotic species with climate change. Am. J. Bot. 100, 1407–1421. https://doi.org/10.3732/ajb.1200478.
Wu, S., Wang, J., Yan, Z., Song, G., Chen, Y., Ma, Q., Deng, M., Wu, Y., Zhao, Y., Guo, Z., Yuan, Z., Dai, G., Xu, X., Yang, X., Su, Y., Liu, L., Wu, J., 2021. Monitoring tree-crown scale autumn leaf phenology in a temperate forest with an integration of PlanetScope and drone remote sensing observations. ISPRS J. Photogramm. Remote Sens. 171, 36–48. https://doi.org/10.1016/j.isprsjprs.2020.10.017.
Xie, Y., Civco, D.L., Silander, J.A., 2018. Species-specific spring and autumn leaf phenology captured by time-lapse digital cameras. Ecosphere 9, e02089. https://doi.org/10.1002/ECS2.2089.
Xie, Y., Wilson, A.M., 2020. Change point estimation of deciduous forest land surface phenology. Remote Sens. Environ. 111698 https://doi.org/10.1016/j.rse.2020.111698.
Yang, Z., Diao, C., Li, B., 2021. A robust hybrid deep learning model for spatiotemporal image fusion. Remote Sens. 13 https://doi.org/10.3390/rs13245005.
Zeng, L., Wardlow, B.D., Xiang, D., Hu, S., Li, D., 2020. A review of vegetation phenological metrics extraction using time-series, multispectral satellite data. Remote Sens. Environ. 237, 111511.
Zhang, C., Marzougui, A., Sankaran, S., 2020. High-resolution satellite imagery applications in crop phenotyping: an overview. Comput. Electron. Agric. https://doi.org/10.1016/j.compag.2020.105584.
Zhang, X., Friedl, M.A., Schaaf, C.B., Strahler, A.H., Hodges, J.C.F., Gao, F., Reed, B.C., Huete, A., 2003. Monitoring vegetation phenology using MODIS. Remote Sens. Environ. 84, 471–475. https://doi.org/10.1016/S0034-4257(02)00135-9.
Zhu, W., Tian, H., Xu, X., Pan, Y., Chen, G., Lin, W., 2011. Extension of the growing season due to delayed autumn over mid and high latitudes in North America during 1982-2006. https://doi.org/10.1111/j.1466-8238.2011.00675.x.